AN INQUIRY INTO THE UNDERSTANDING OF THE EXAFS AS

A TOOL FOR THE STRUCTURAL INVESTIGATION

OF DISORDERED SYSTEMS

by

Daniel J. Kay

B.Sc., University of Florida, 1966

A THESIS SUBMITTED IN PARTIAL FULFILLMENT OF

THE REQUIREMENTS FOR THE DEGREE OF

MASTER OF SCIENCE

in the Department

of

Physics

APPROVAL

Name: Daniel J. Kay

Degree: Master of Science

Title of Thesis: An Inquiry into the Understanding of the
                   EXAFS as a Tool for the Structural
                   Investigation of Disordered Systems

Examining Committee:

   Chairman: S. Gygax

_____
M. Plischke
Senior Supervisor

_____
L. Ballentine

_____
Crozier

_____
K. Rieckhoff
External Examiner
Professor
Department of Physics
Simon Fraser University

Date Approved: _____

Title of Thesis/Dissertation:

An Inquiry into the Understanding of the EXAFS

as a Tool for the Structural Investigation of

Disordered Systems

Author:

(signature)

Daniel J. Kay

(name)

1978-12-11

(date)

ABSTRACT

The extended X-ray absorption fine structure (EXAFS) is calculated for two models for disordered systems: (1) a continuous-random-network model for semiconductors; and (2) a dense-random-packing-of-hard-spheres model for metallic systems. The EXAFS is analyzed via the Fourier Transform. Multiple scattering and asymmetry of real-space distributions are considered as to their effects on the analysis of the EXAFS.

It is shown that there are serious limitations to the analysis of the EXAFS which center around the inability to interpret the spectrum for sufficiently low energies. It is further shown that, because of these limitations, the technique, using the current methods of analysis, is of limited usefulness for distinguishing between different structural models for a particular system.

Acknowledgements

I wish to express my deepest appreciation to my supervisor, Mike Plischke, for helping me to find my way through all this. Mike also supplied the program for generating hard-sphere clusters.

I gratefully acknowledge many conversations with Daryl Crozier on various aspects of the EXAFS, especially the analysis of experimental data. I also want to thank David Zobin for his help and encouragement.

The coordinates for the Germanium cluster were supplied by Dave Beeman of Harvey Mudd College in Claremont, California.

Thanks also to Doreen Grant for her typewriter magic (and to Jo-Ann Murphy who pinch hit when Doreen split for Hawaii).

TABLE OF CONTENTS

Page

LIST OF TABLES

LIST OF FIGURES

Chapter I - Introduction

When a beam of monochromatic X-rays is passed through matter it is observed that the beam is attenuated with increasing absorber thickness. With the assumption that the decrease in intensity of the incident X-ray beam is proportional to the intensity one obtains the relation

$$I(x) = I_o e^{-\mu x} , \qquad (1.1)$$

where I_o is the incident intensity, x the absorber thickness, and μ the monochromatic linear absorption coefficient. In general, μ is a function of X-ray energy.

The linear absorption coefficient can be calculated by relating it to the atomic absorption coefficient σ_T, which is μ divided by the number density of atoms, i.e. the number of atoms per unit length and per unit cross-section of the beam:

$$\mu = n \, \sigma_T. \qquad (1.2)$$

Thus σ_T is the total interaction cross-section for absorption.

The absorption spectra of most condensed materials (as a function of energy) are distinguished by several absorption edges, abrupt rises in the absorption coefficient at energies just sufficient to eject an inner electron from its atom. Beyond an edge spectra show a monotonic decrease until the next ionization energy is reached.

On closer inspection absorption spectra are seen to deviate from the simple behavior described above. The abrupt rise in absorption at an edge is not quite so sharp - and the spectrum on the high-energy side of an edge exhibits an oscillatory fine structure (Figure 1.1). Beyond about 50 e.v. above the edge this is referred to as the extended X-ray absorption fine structure (EXAFS).

The history of attempts to understand the EXAFS was reviewed by Azároff (1963). It was Kronig (1931) who presented the first theory. In accord with the then recently discovered band theory of solids, Kronig proposed that the energy of the emitted photoelectron should correspond to an allowed or a forbidden transition. The former would lead to maxima in the absorption spectrum while the latter would lead to minima. In this model the photoelectron is described by a Bloch function. In a second paper Kronig (1932a) used this idea to present a detailed analysis of the problem. He was able to predict energies at which anomalies should occur in the absorption spectrum, provided the average inner potential of the crystal is known. Agreement with experimental data on Cu is considered fair.

Kronig's approach is based upon the existence of long-range order (LRO) in a crystal. Oscillations in the absorption spectrum are seen to result from the density of states distributions grouped into allowed and forbidden energy bands. He assumed that the transition probabilities for the ejected photoelectron did not vary significantly with energy.

In a third paper, Kronig (1932b) took a different approach to the problem. He analyzed a diatomic molecule, considering the potential field of the molecule as a whole so that the one-electron approximation could be used. The transition probabilities for the photoelectron may then be
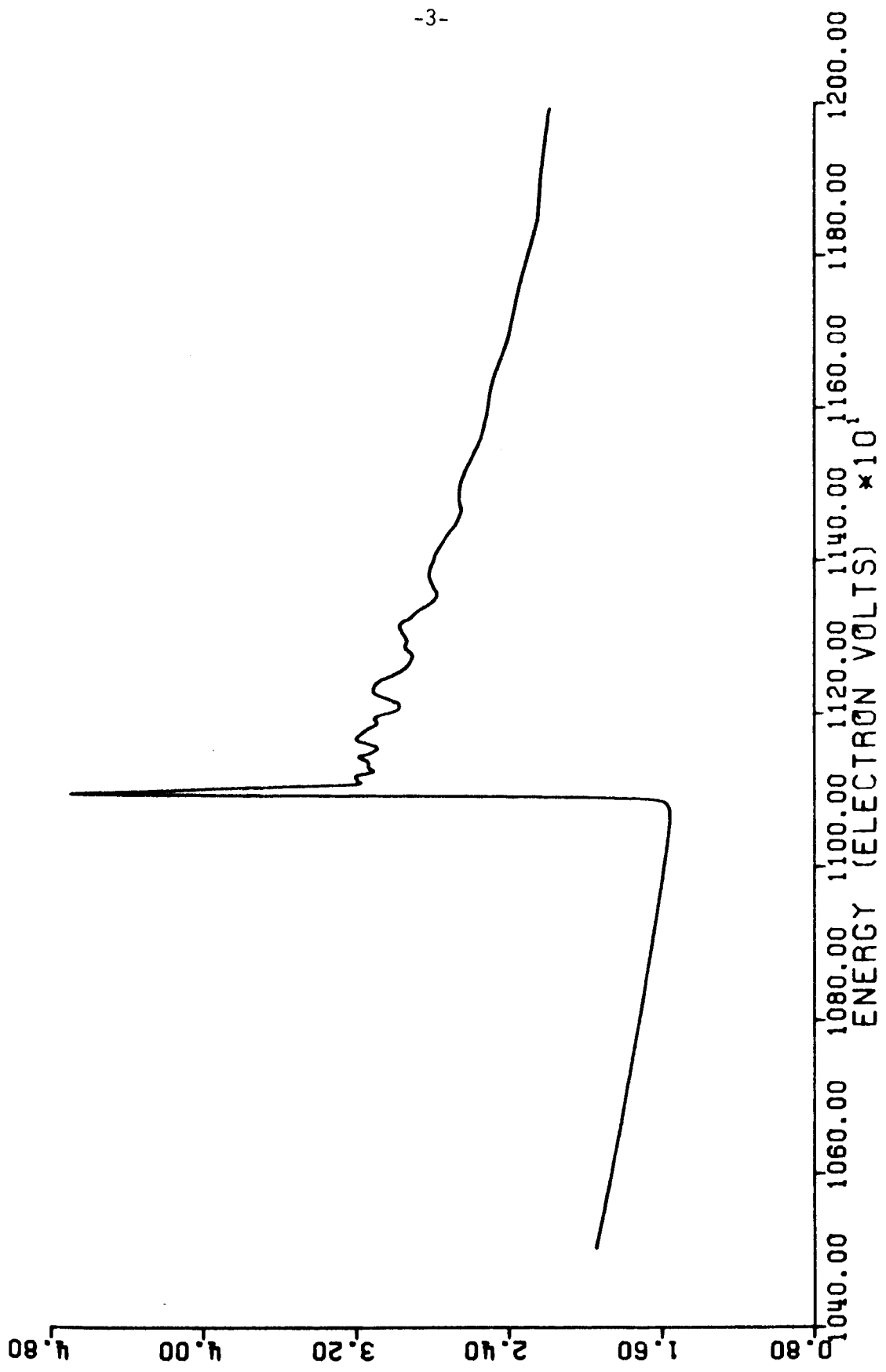
Figure 1.1. Ratio of incident X-ray intensity to measured intensity (I_0/I) as a function of energy for crystalline Ge at 20°C (E.D. Crozier, unpublished).

calculated. This requires an analysis of the effects of the scattering of the photoelectron by the surrounding atoms.

Most later theories have followed this short-range order (SRO) approach. Shiraiwa et al. (1958) pointed out that because of elastic and inelastic scattering the photoelectron travels only a few lattice spacings before the amplitude becomes nearly zero. From this point of view only the nearest neighbors of the absorbing atom need be considered in the theory.

Various theories involving SRO (Peterson, 1933; Kostarev, 1949; Shiraiwa et al., 1958) have been used to calculate the oscillatory part of the absorption curves, χ, essentially equivalent to

$$\chi(k) \propto - \sum_i \frac{N_i}{r_i^2} \sin(2kr_i + 2\delta), \tag{1.3}$$

where N_i is the number of atoms in the ith shell at a distance r_i from the absorbing atom; δ is the phase of the ejected electron wave. The idea is very simple. The photoelectron wave is scattered by the atoms surrounding the absorbing atom. The absorption then depends upon the interference between the outgoing and incoming photoelectron states at the absorbing atom. The SRO theories differ mainly in how the potentials of the scattering atoms are calculated, and in the formalism used to determine the phases of the scattered waves.

Azároff (1963) compared the various theories with existing experimental data and concluded that none of them explained the observed fine structure in full detail. A difficulty in comparing theories at this time was the lack of good experimental data beyond a few hundred electron volts above the edge.

The most recent and successful theory of the EXAFS is based on SRO and is due to Sayers et al. (1970). They assume that the oscillatory behavior of the EXAFS is due solely to photoelectric absorption and calculate, therefore, the photoabsorption cross-section. They treat the ejected electron as a spherical wave which expands about the absorbing atom and is partially scattered by the surrounding atoms which are treated as point scatterers. The EXAFS is determined from the transition matrix between an initial K state and the final photoelectron state, neglecting multiple scattering. They arrive at a formula similar to Eqn. 1.3:

$$\chi(k) = -\frac{1}{k} \sum_{j} \frac{N_j e^{-\gamma r_j}}{r_j^2} e^{-\frac{1}{2}\sigma_j^2 k^2} \sin(2kr_j + 2\eta(k)), \qquad (1.4)$$

where γ^{-1} is an empirical mean free path parameter (used essentially to account for multiple scattering effects), η is the phase shift due to the potential of the absorbing atom, and σ_j^2 is the mean square deviation of the positions of the atoms in the jth shell about their average position due to thermal disorder. Their theoretical calculations on crystalline Cu, Fe and Ge produced curves which are in good general agreement with experimental data over an energy range of 100 - 600 e.v.

More recent theories (Stern, 1974; Ashley and Doniach, 1975; Lee and Pendry, 1975) are essentially refinements of that of Sayers et al. In particular, the δ-function potentials have been replaced by muffin tins, and multiple scattering has been treated.

In a later paper Sayers et al. (1971) showed how to invert Eqn. 1.4 to obtain a model structure function which contains information on the number, distance to and distribution of atoms surrounding the absorbing atom. Forty years of research bears fruit! The EXAFS presents itself as a potentially powerful technique for the investigation of amorphous materials.

Structural information on amorphous materials comes through X-ray, neutron and electron scattering measurements. Experimental data is converted into a radial distribution function which is an average over all atomic species present. The EXAFS, on the other hand, yields a structure function which contains information on the environment of a single type of atom. Since absorption edges usually occur at easily separable values of ionization energy, the structure above each appropriate edge (and thus the environment of each atomic species) can be separately studied in a complex material.

The purpose of this thesis is to investigate the usefulness of the EXAFS as a tool for understanding the structure of disordered systems. In particular we intend to discover some of the limitations of the EXAFS analysis by means of model calculations. Since model building itself is an investigative tool, we can also inquire into the ability of the EXAFS technique to distinguish between different models. It may then be possible to use the EXAFS to eliminate inappropriate models.

We begin, in Chapter 2, with the development of the EXAFS formalism using the Green's function approach. Chapter 3 then discusses the structure of amorphous materials, dealing particularly with the concept of model building. In Chapter 4 we apply the EXAFS formalism to a continuous-random-

network (CRN) model for amorphous semiconductors. In particular we investigate the Fourier Transform analysis of the EXAFS, and we make a comparison with some experimental data. Chapter 5 deals with a dense-random-packing-of-hard-spheres model for metallic systems. Beyond the Fourier analysis we also consider the effects of multiple scattering and asymmetric distributions on the analysis of the EXAFS. In the final chapter we summarize our work and draw some conclusions.

Chapter 2 - EXAFS Formalism

In this chapter we develop the formalism for calculating the EXAFS following the approach of Ashley and Doniach (1975). (For a general discussion of scattering theory see Messiah, 1962, chapters X and XIX or Roman, 1965, chapters 3 and 4.) In section 2.1 the problem is divided into two parts: (1) the effect of the potential of the absorbing atom on the emitted photoelectron; and (2) the behavior of the emitted photoelectron as it moves through the solid. The normalized oscillatory part of the absorption spectrum is then calculated in section 2.2 using Green's functions. In section 2.3 a simple analytic expression is derived in the high-energy approximation. Attenuation and thermal effects are considered in section 2.4. Section 2.5 is devoted to the Fourier-Transform technique for analyzing the EXAFS. Finally, a brief summary is contained in section 2.6.

Section 2.1 - Definition of the Problem

The photoelectric absorption cross-section, in the dipole approximation (Bethe and Salpeter, 1957, secs. 59 and 69), is given by

$$\sigma_a = \frac{4}{3}\pi^2\alpha(h\nu)\sum_f |<f|\underline{r}|i>|^2 \; \delta(E_i + h\nu - E_f), \tag{2.1}$$

where α is the fine structure constant, $h\nu$ the photon energy, $|i>$ the initial core state of the electron, and $|f>$ the final photoelectron state which must be calculated from a model of the potential. The potential is represented by a system of spherically-symmetric, non-overlapping,

spin-independent muffin tin potentials. The zero of energy is determined by the (assumed) constant potential between muffin tins.

We pause here to state more explicitly the approximations contained in the preceding paragraph. First, this is a one-electron model. It is not valid close to the edge where many body effects are expected to be important. This is why one refers to the _extended_ fine structure. Second, the effect of the potential on the ejected photoelectron is not a static problem. The ionized atom is in an excited state and a many-electron relaxation process takes place. If, as in a metal, the relaxation time is short compared to the lifetime of the excited state, a screened Coulomb potential may be used. In an insulator the relaxation time is long and the spectrum will be Coulomb-like near the edge. We neglect relaxation effects and take the effective single-particle potential to be a screened core hole. Phase shift analysis may then be applied.

Since the model potential is spherically symmetric, it is convenient to use the angular momentum representation. We can then decompose the electron states into partial wave states. Let

$$\phi_L^E(\underline{r}) = i^\ell R_\ell^E(r) Y_L(\hat{r}) \qquad (2.2)$$

be a complete set of one-center basis functions. $Y_L(\hat{r})$ are the usual spherical harmonics and the index L is taken to represent both angular momentum indices ℓ and m. $R_\ell^E(r)$ are solutions of the Schrödinger equation at energy E for the potential of the absorbing atom in the absence of the other potentials.

Outside the muffin tin the radial wavefunctions must be of the form (Messiah, 1962, p. 390)

$$R_\ell^E(r) = A_\ell (j_\ell(kr) \cos \delta_\ell - n_\ell(kr) \sin \delta_\ell)$$

$$= \frac{1}{2} A_\ell (h_\ell^{(-)}(kr) e^{-i\delta_\ell} + h_\ell^{(+)}(kr) e^{i\delta_\ell}), \qquad (2.3)$$

where j, n, $h^{(-)}$, $h^{(+)}$ are the spherical Bessel and Hankel functions, A_ℓ the normalization constant, $k = \sqrt{2mE/\hbar^2}$, and δ_ℓ is the phase shift due to the potential. Note that the effect of the potential of the absorbing atom is to introduce a phase difference of $e^{2i\delta_\ell}$ between incoming and outgoing waves.

Denote the core state by

$$|i\rangle = \phi_{L_c}(\underline{r}) = i^{\ell_c} R_c(r) Y_{L_c}(\hat{r}). \qquad (2.4)$$

For small values of ℓ_c the core state will be highly localized near the origin. Assume that $R_c(r) = 0$ beyond the muffin tin radius R_{MT}. Then

$$\int_0^{R_{MT}} r^2 dr \, R_c^2(r) = 1. \qquad (2.5)$$

Expand the final states in the usual way as

$$|f\rangle = \sum_L |\phi_L^E(\underline{r})\rangle\langle\phi_L^E(\underline{r})|f\rangle. \qquad (2.6)$$

Note that

$$E = E_i + h\nu. \tag{2.7}$$

Then we may write Eqn. 2.1 as

$$\sigma_a = \frac{4}{3}\pi^2 \alpha(h\nu) \sum_f \sum_L <f|\phi_L^E(\underline{r})><\phi_L^E(\underline{r})|\underline{r}|\phi_{L_c}(\underline{r})>$$

$$\times \sum_{L'} <\phi_{L_c}(\underline{r})|\underline{r}|\phi_{L'}^E(\underline{r})><\phi_{L'}^E(\underline{r})|f> \delta(E - E_f)$$

$$= \frac{4}{3}\pi^2 \alpha(h\nu) \sum_{LL'} <\phi_L^E(\underline{r})|\underline{r}|\phi_{L_c}(\underline{r})><\phi_{L_c}(\underline{r})|\underline{r}|\phi_{L'}^E(\underline{r})>$$

$$\times <\phi_{L'}^E(\underline{r})|(\sum_f |f> \delta(E - E_f)<f|)|\phi_L^E(\underline{r})>. \tag{2.8}$$

The δ-function in Eqn. 2.8 may be defined (Messiah, 1962, p. 469) by

$$\delta(E - E_f) = -\frac{1}{\pi} \lim_{\varepsilon \to 0^+} \text{Im} \frac{1}{E - E_f + i\varepsilon}. \tag{2.9}$$

Since $|f>$ are the eigenstates of the complete Hamiltonian H, the sum over f in Eqn. 2.8 is the spectral representation of the operator $-\frac{1}{\pi} \lim_{\varepsilon \to 0^+} \text{Im} \frac{1}{E - H + i\varepsilon}$. And this operator is the Green's function $G^{(+)}$ in the presence of the full potential (Messiah, 1962, p. 819). Thus

$$\sigma_a = -\frac{1}{\pi} \text{Im} \sum_{LL'} M_{LL'}^{core} <\phi_{L'}^E(\underline{r})|G^{(+)}|\phi_L^E(\underline{r})>, \tag{2.10}$$

where

$$M_{LL'}^{core} = \frac{4}{3}\pi^2 \alpha(h\nu)<\phi_L^E(\underline{r})|\underline{r}|\phi_{L_c}(\underline{r})><\phi_{L_c}(\underline{r})|\underline{r}|\phi_{L'}^E(\underline{r})>. \tag{2.11}$$

The angular integrations in Eqn. 2.11 are easily performed by expressing $\underline{r}$ in spherical harmonics. This gives integrals like

$$\int d\Omega Y_\ell^{m_c}{}^* \; Y_\ell^m \; Y_1^{-1,0,1} \quad , \tag{2.12}$$

which are Gaunt coefficients (Appendix A). These lead to the selection rules $\delta_{m_c,m}$, $\delta_{m_c\pm 1,m}$, $\delta_{\ell_c\pm 1,\ell}$. Let $C(L,L')$ denote the numerical value of the integral. Then

$$M_{LL'}^{core} = \frac{4}{3}\pi^2 \alpha(h\nu) C(L,L') \delta_{\ell,\ell_c\pm 1} \; \delta_{\ell;\ell_c\pm 1} \; I_{LL'}^{core} \quad , \tag{2.13}$$

where

$$I_{LL'}^{core} = \left\{ \int r^3 dr R_c(r) R_\ell^E(r) \right\} \left\{ \int r^3 dr R_c(r) R_{\ell'}^E(r) \right\} \quad . \tag{2.14}$$

The problem has now been divided into two parts. The matrix elements of the Green's function $G^{(+)}$ determine the behavior of the photoelectron outside the central atom as it propagates through the muffin tin system. The effect of the potential of the absorbing atom on the emitted photo-electron is represented by $M_{LL'}^{core}$.

Section 2.2 - Calculation of the EXAFS

The basic mathematical idea we use is the representation of a region of space (the muffin tin sphere) by a black box, the properties of which are determined by parameters which describe conditions at the boundary of the region. For a spherically-symmetric potential these parameters are the

phase shifts of the partial waves.

We must calculate the Green's function matrix elements of Eqn. 2.10. This problem has been formulated by Beeby (1964). The chief mathematical tool we employ is the T-matrix defined by

$$\langle \varphi_b | T | \varphi_a \rangle = \langle \varphi_b | V | \psi_a^{(+)} \rangle \, , \tag{2.15}$$

where $\psi_a^{(+)}$ is the stationary solution to the full Hamiltonian with wave vector $\underline{k}_a$ and φ_a is a plane wave with the same wave vector. Formally

$$T = V + VG^\circ T \, , \tag{2.16}$$

where G° is the free space Green's function.

Consider a system of potentials V_α centered on sites $\underline{R}_\alpha$. Let t_α be the T-matrix corresponding to the single potential V_α so that

$$t_\alpha(\underline{x},\underline{y}) = V_\alpha(\underline{x}) \, \delta \, (\underline{x} - \underline{y}) + \int d\underline{z} V_\alpha(\underline{x}) G^\circ(\underline{x},\underline{z}) t_\alpha(\underline{z},\underline{y}) \, . \tag{2.17}$$

The full T-matrix is

$$T = \sum_\alpha t_\alpha + \sum_{\alpha \neq \beta} t_\alpha G^\circ_{\alpha\beta} t_\beta + \sum_{\substack{\alpha \neq \beta \\ \beta \neq \nu}} t_\alpha G^\circ_{\alpha\beta} t_\beta G^\circ_{\beta\nu} t_\nu + \ldots \quad . \tag{2.18}$$

The restrictions on the sums in Eqn. 2.18 insure that successive scattering from the same potential does not occur.

The full Green's function is then

$$G_{\alpha\nu}(\underline{r},\underline{r}') \;=\; G^{\circ}_{\alpha\nu}(\underline{r},\underline{r}') \;+\; \sum_{\beta}\iint d\underline{r}_1 d\underline{r}_2 G^{\circ}_{\alpha\beta}(\underline{r},\underline{r}_1) t_{\beta}(\underline{r}_1,\underline{r}_2) G^{\circ}_{\beta\nu}(\underline{r}_2,\underline{r}')$$

$$+\; \sum_{\beta,\delta}\iiiint d\underline{r}_1 d\underline{r}_2 d\underline{r}_3 d\underline{r}_4 G^{\circ}_{\alpha\beta}(\underline{r},\underline{r}_1) t_{\beta}(\underline{r}_1,\underline{r}_2) G^{\circ}_{\beta\delta}(\underline{r}_2,\underline{r}_3) t_{\delta}(\underline{r}_3,\underline{r}_4) G^{\circ}_{\delta\nu}(\underline{r}_4,\underline{r}')$$

$$+\; \ldots \quad . \tag{2.19}$$

This represents the propagation from $\underline{r}$ near $\underline{R}_{\alpha}$ to $\underline{r}'$ near $\underline{R}_{\nu}$. The first term is the direct free propagation. The second term is the propagation from $\underline{r}$ to $\underline{r}'$ by way of a single scattering by a potential at $\underline{R}_{\beta}$. The next term is the double scattering contribution, and so on.

Let $\underline{r}_{\alpha}$ denote a coordinate measured relative to $\underline{R}_{\alpha}$ so that $\underline{r} = \underline{R}_{\alpha} + \underline{r}_{\alpha}$ and $\underline{r}' = \underline{R}_{\nu} + \underline{r}_{\nu}$. Further set $\underline{R}_{\alpha\nu} = \underline{R}_{\nu} - \underline{R}_{\alpha}$. The free electron Green's function is

$$G^{\circ}(\underline{r},\underline{r}') \;=\; -\frac{1}{4\pi}\,\frac{e^{ik|\underline{r}-\underline{r}'|}}{|\underline{r}-\underline{r}'|} \;, \tag{2.20}$$

$$G^{\circ}_{\alpha\nu}(\underline{r},\underline{r}') \;=\; -\frac{1}{4\pi}\,\frac{e^{ik|\underline{r}_{\alpha}-\underline{r}_{\nu}-\underline{R}_{\alpha\nu}|}}{|\underline{r}_{\alpha}-\underline{r}_{\nu}-\underline{R}_{\alpha\nu}|} \;. \tag{2.21}$$

The Newmann expansion of Eqn. 2.21 (Messiah, 1962, p. 497) is

$$G^{\circ}_{\alpha\nu}(\underline{r},\underline{r}') \;=\; -k\sum_{L} H_{L}(\underline{r}_{\alpha} - \underline{R}_{\alpha\nu}) J_{L}{}^{*}(\underline{r}_{\nu}) \;, \tag{2.22}$$

where

$$J_L(\underline{r}) = i^\ell j_\ell(kr)Y_L(\hat{r}) ,$$

$$H_L(\underline{r}) = i^{\ell+1} h_\ell^{(+)}(kr)Y_L(\hat{r}) . \tag{2.23}$$

A useful identity (Lloyd and Smith, 1972) is

$$H_L(\underline{r}_\alpha - \underline{R}_{\alpha\nu}) = 4\pi \sum_{L_1 L_2} C_{L L_1 L_2} H_{L_1}(-\underline{R}_{\alpha\nu}) J_{L_2}(\underline{r}_\alpha) ,$$

$$|\underline{r}_\alpha| < |\underline{R}_{\alpha\nu}| , \tag{2.24}$$

where

$$C_{L L_1 L_2} = \int d\Omega Y_L^* Y_{L_1} Y_{L_2}$$

are Gaunt coefficients. Then Eqn. 2.22 may be written

$$G_{\alpha\nu}^\circ(\underline{r},\underline{r}') = \sum_{LL'} G_{LL'}^\circ(\underline{R}_\alpha,\underline{R}_\nu) J_L(\underline{r}_\alpha) J_{L'}^*(\underline{r}_\nu), \tag{2.25}$$

where

$$G^\circ_{LL'}(\underline{R}_\alpha,\underline{R}_\nu) = -\pi 4k \sum_{L_1} C_{L' L_1 L} H_{L_1}(-\underline{R}_{\alpha\nu}) . \tag{2.26}$$

We note here, for future reference, that since for all ℓ

$$[i^{\ell+1} h_\ell^{(+)}(kr)] \xrightarrow[kr\to\infty]{} \frac{e^{ikr}}{r} , \tag{2.27}$$

asymptotically we have

$$G^{\circ}_{LL'}(\underline{R}_\alpha,\underline{R}_\nu) = -4\pi \left(\frac{e^{ikR_{\alpha\beta}}}{R_{\alpha\beta}}\right) \sum_{L_1} C_{L'L_1 L} Y_{L_1}(-\hat{R}_{\alpha\beta}). \tag{2.28}$$

To evaluate the full Green's function it is obviously convenient to expand the T-matrix in spherical haromonics which, for a spherically-symmetric potential, may be written

$$t(\underline{x},\underline{y}) = \sum_L t_\ell(x,y)\{i^\ell Y_L(\hat{x})\}\{i^\ell Y_L(\hat{y})\}^*. \tag{2.29}$$

Using Eqns. 2.29 and 2.25 the Green's function (Eqn. 2.19) is

$$G_{\alpha\nu}(\underline{r},\underline{r}') = \sum_{LL'} G^{\circ}_{LL'}(\underline{R}_\alpha,\underline{R}_\nu) J_L(\underline{r}_\alpha) J_{L'}^*(\underline{r}_\nu)$$

$$+ \sum_\beta \iint dr_\beta dr'_\beta \left[\sum_{LL_1} G^{\circ}_{LL_1}(\underline{R}_\alpha,\underline{R}_\beta) J_L(\underline{r}_\alpha) J_{L_1}^*(\underline{r}_\beta)\right]$$

$$\times \left[\sum_{L_2} t^{\beta}_{\ell_2}(\underline{r}_\beta,\underline{r}'_\beta)(i^{\ell_2} Y_{L_2}(\hat{r}_\beta))(i^{\ell_2} Y_{L_2}(\hat{r}'_\beta))^*\right]$$

$$\times \left[\sum_{L_3 L'} G^{\circ}_{L_3 L'}(\underline{R}_\beta,\underline{R}_\nu) J_{L_3}(\underline{r}'_\beta) J_{L'}^*(\underline{r}_\nu)\right] + \ldots \quad . \tag{2.30}$$

the angular integrations of Eqn. 2.30 give terms like

$$\int d\Omega_\beta [i^{\ell_1} Y_{L_1}(\hat{r}_\beta)]^* [i^{\ell_2} Y_{L_2}(\hat{r}_\beta)] = \delta_{L_1,L_2}, \tag{2.31}$$

using the orthonormality property of the spherical harmonics.

Further simplification occurs by defining a momentum space t-function by the transform

$$t_\ell(p,q) = \iint x^2 dx\, y^2 dy\, j_\ell(px) t_\ell(x,y) j_\ell(qy). \tag{2.32}$$

We note here that the t-function is related to the phase shifts (Messiah, 1962, p. 818) by

$$t_\ell(k,k) \equiv t_\ell(k) = -\frac{1}{k} \sin\delta_\ell\, e^{i\delta_\ell} \tag{2.33}$$

Using Eqns. 2.32 and 2.31 the Green's function (Eqn. 2.30) becomes

$$G_{\alpha\nu}(\underline{r},\underline{r}') = \sum_{LL'} G_{LL'}(\underline{R}_\alpha,\underline{R}_\nu) J_L(\underline{r}_\alpha) J_{L'}^*(\underline{r}_\nu), \tag{2.34}$$

where

$$G_{LL'}(\underline{R}_\alpha,\underline{R}_\nu) = G_{LL'}^\circ(\underline{R}_\alpha,\underline{R}_\nu) + \sum_{\beta\neq\alpha} \sum_{L_1} (\underline{R}_\alpha,\underline{R}_\beta) t_{\ell_1}^\beta(k,k) G_{L_1 L'}^\circ(\underline{R}_\beta,\underline{R}_\nu)$$

$$+ \sum_{\substack{\beta\neq\alpha \\ \delta\neq\beta}} \sum_{L_1 L_2} G_{LL_1}^\circ(\underline{R}_\alpha,\underline{R}_\beta) t_{\ell_1}^\beta(k,k) G_{L_1 L_2}^\circ(\underline{R}_\beta,\underline{R}_\delta) t_{\ell_2}^\delta(k,k) G_{L_2 L'}^\circ(\underline{R}_\delta,\underline{R}_\nu)$$

$$+ \ldots \tag{2.35}$$

$$= G_{LL'}^\circ(\underline{R}_\alpha,\underline{R}_\nu) + \sum_{\beta\neq\alpha} \sum_{L_1} G_{LL_1}(\underline{R}_\alpha,\underline{R}_\beta) t_{\ell_1}^\beta(k) G_{L_1 L'}^\circ(\underline{R}_\beta,\underline{R}_\nu). \tag{2.36}$$

Since we have assumed that the core state is highly localized near the origin, Eqn. 2.36 is evaluated at $\underline{r} = 0$. The 'desired' matrix elements are then

$$G_{LL'}(\underline{R}_\alpha, \underline{R}_\alpha) = G^\circ_{LL'}(\underline{R}_\alpha, \underline{R}_\alpha) + \sum_{\beta \neq \alpha} \sum_{L_1} G_{LL_1}(\underline{R}_\alpha, \underline{R}_\beta) t^\beta_{\ell_1}(k) G^\circ_{L_1 L'}(\underline{R}_\beta, \underline{R}_\alpha).$$

(2.37)

The first term gives the atomic photoelectric effect (no scattering). The second term represents an outgoing L wave which returns as an incoming L' wave after being scattered by atoms located at $\underline{R}_\beta$. The effect of the absorbing atom is to shift the phase between the outgoing L wave and incoming L' wave by $\eta_\ell + \eta_{\ell'}$. (The phase shift of the absorbing atom will be denoted by η to distinguish it from the phase shifts δ of undisturbed atoms.)

We can now evaluate the cross section (Eqn. 2.10) and calculate the absorption coefficient. We calculate the normalized oscillatory part of the spectrum by

$$\chi(k) = \frac{\mu - \mu_0}{\mu_0} = \frac{\sigma_a - \sigma_a^{atomic}}{\sigma_a^{atomic}}$$

(2.38)

$$= \frac{\text{Im} \sum_{m_\ell, m_{\ell'}} M^{core}_{11} e^{i(\eta_\ell + \eta_{\ell'})} \sum_{\beta \neq \alpha} \sum_{L_1} G_{1L_1}(\underline{R}_\alpha, \underline{R}_\beta) t^\beta_{\ell_1}(k) G^\circ_{L_1 1}(\underline{R}_\beta, \underline{R}_\alpha)}{\text{Im} \sum_{m_\ell, m_{\ell'}} M^{core}_{11} G^\circ_{11}(\underline{R}_\alpha, \underline{R}_\alpha)}$$

(2.39)

Here we have assumed that the core state is an 's wave' so that $\ell_c = 0$. The dipole selection rules (Eqn. 2.13) require $\ell = \ell' = 1$.

To evaluate the denominator of Eqn. 2.39 we employ the Newmann expansion (Eqn. 2.26) to give

$$\sigma_a^{atomic} = Im \sum_{m_\ell, m_{\ell'}} M_{11}^{core} \left\{ -4\pi k \sum_{L_1} C_{1L_1 1} \, i^{\ell_1+1} \, Y_{L_1}(\hat{0}) h_{\ell_1}^{(+)}(0) \right\} . \tag{2.40}$$

The Gaunt coefficient $C_{1L_1 1}$ is non zero only if ℓ_1 is 0 or 2 (Eqn. A.2). Since

$$h_\ell^{(+)}(kr) = j_\ell(kr) + in_\ell(kr), \tag{2.41}$$

and ℓ_1 is even,

$$\sigma_a^{atomic} = -4\pi k \sum_{m_\ell, m_{\ell'}} M_{11}^{core} \left\{ C_{101} Y_0 j_0(0) + \sum_{m_2} C_{121} Y_2(\hat{0}) j_2(0) \right\}$$

$$= -k \sum_{m_\ell, m_{\ell'}} M_{11}^{core} . \tag{2.42}$$

To simplify the analytical evaluation of Eqn. 2.39 we assume that, asymptotically, the photoelectron is spherically symmetric about the absorbing atom so that G_{1L_1} becomes G_{0L_1}. Then $m_\ell = m_{\ell'} = 0$, the sums over m_ℓ and $m_{\ell'}$ disappear, and M_{11}^{core} cancels. The normalized oscillatory part of the X-ray absorption spectrum is then

$$\chi(k) = -\frac{1}{k} Im \left\{ e^{2i\eta_1} \sum_{\beta \neq \alpha} \sum_L G_{0L}(\underline{R}_\alpha, \underline{R}_\beta) t_\ell^\beta(k) G_{L0}^\circ(\underline{R}_\beta, \underline{R}_\alpha) \right\} . \tag{2.43}$$

We emphasize here that scattering to all orders is included in Eqn. 2.43 through the full Green's function G_{0L}.

Section 2.3 - High Energy Approximation

The amount of scattering at a given site, as represented by the t-function, decreases with increasing energy (Eqn. 2.33). Thus for sufficiently high energy (determined by such factors as atomic species and structure) the dominant contribution to the EXAFS is that of singly-scattered waves.

We obtain the single-scattering contribution to the EXAFS by replacing the full Green's function G in Eqn. 2.43 by the free Green's function G°:

$$\chi(k) \;=\; -\frac{1}{k} \, \text{Im} \left\{ e^{2i\eta_1} \sum_{\beta \neq \alpha} \sum_{L} G^{\circ}_{0L}(\underline{R}_\alpha, \underline{R}_\beta) t^{\beta}_{\ell}(k) G^{\circ}_{L0}(\underline{R}_\beta, \underline{R}_\alpha) \right\} . \qquad (2.44)$$

The asymptotic form of G° (Eqn. 2.28) can be used. The smallest inter-atomic distance we encounter is $r \approx 2.5 \text{A}^\circ$, so for $k > 4\text{A}^{\circ -1}$ ($E \gtrsim 60$ e.v.) this will be a good approximation. Eqn. 2.44 then becomes

$$\chi(k) \;=\; -\frac{1}{k} \, \text{Im} \left\{ e^{2i\eta_1} \sum_{\beta \neq \alpha} \frac{e^{2ikR_{\alpha\beta}}}{R_{\alpha\beta}^{2}} (4\pi)^2 \sum_{L} t^{\beta}_{\ell}(k) \sum_{L_1} C_{LL_1 0} Y_{L_1}(-\hat{R}_{\alpha\beta}) \right.$$

$$\left. \times \sum_{L_2} C_{0L_2 L} Y_{L_2}(-\hat{R}_{\beta\alpha}) \right\} . \qquad (2.45)$$

Using the properties of the Gaunt coefficients (Eqn. A.3) we have

$$\chi(k) \;=\; -\frac{1}{k} \, \text{Im} \left\{ \sum_{\beta \neq \alpha} \frac{e^{i(2\eta_1 + 2kR_{\alpha\beta})}}{R_{\alpha\beta}^{2}} 4\pi \sum_{L} t^{\beta}_{\ell}(k)(-1)^m Y_{\ell,m}(-\hat{R}_{\alpha\beta}) Y_{\ell,-m}(-\hat{R}_{\beta\alpha}) \right\}$$
$$\qquad (2.46)$$

$$=\; -\frac{1}{k} \, \text{Im} \left\{ \sum_{\beta \neq \alpha} \frac{e^{i(2\eta_1 + 2kR_{\alpha\beta})}}{R_{\alpha\beta}^{2}} \sum_{\ell} t^{\beta}_{\ell}(k)(2\ell+1) P_{\ell}(\cos\pi) \right\} , \qquad (2.47)$$

applying the addition theorem for spherical harmonics (Messiah, 1962, p. 496)

$$P_\ell(\hat{r}' \cdot \hat{r}) = \frac{4\pi}{2\ell+1} \sum_{m=-\ell}^{\ell} (-1)^m Y_{\ell,-m}(\hat{r}') Y_{\ell,m}(\hat{r}). \qquad (2.48)$$

Finally, we express $t_\ell(k)$ in terms of the phase shifts (Eqn. 2.33) and define the scattering amplitude in the usual way (Messiah, 1962, p. 386),

$$f(\theta) = \frac{1}{k} \sum_\ell (2\ell+1) e^{i\delta_\ell} \sin\delta_\ell P_\ell(\cos\theta), \qquad (2.49)$$

to obtain

$$\chi(k) = \frac{1}{k} \operatorname{Im} \left\{ \sum_{\beta \neq \alpha} \frac{e^{i(2\eta_1 + 2kR_{\alpha\beta})}}{R_{\alpha\beta}^2} f_\beta(\pi) \right\}. \qquad (2.50)$$

If the magnitude and phase of the backscattering amplitude are expressed as

$$f_\beta(\pi) = |f_\beta(\pi)| e^{i\theta_\beta}, \qquad (2.51)$$

we obtain the particularly simple expression

$$\chi(k) = \frac{1}{k} \sum_{\beta \neq \alpha} |f_\beta(\pi)| \frac{\sin(2kR_{\alpha\beta} + 2\eta_1 + \theta_\beta)}{R_{\alpha\beta}^2}. \qquad (2.52)$$

Section 2.4 - Attenuation and Thermal Effects

Sayers et al. (1970), in their point-scattering theory, introduce an empirical damping factor $e^{-R/\lambda}$ to attentuate the amplitude of the outgoing photoelectron wave. The parameter λ is the mean free path of the electron. They find that, in the high-energy region of interest, $\lambda \approx 3A^\circ$ gives the best fit to their data. Inelastic scattering mechanisms are expected to give $\lambda \approx 10A^\circ$ so that elastic mechanisms are assumed to dominate. The damping parameter thus functions chiefly as a multiple scattering correction.

This formulation has the disadvantage of containing an adjustable parameter. Ashley and Doniach (1975) have shown how to calculate an attenuation coefficient. To see this, consider a crystalline structure so that we may view each atom as being surrounded by spherical shells j. A spherically-averaged transmission function may be calculated for each shell by

$$T_j(k) = 1 - \frac{N_j \sigma_T(k)}{4\pi R_j^2} , \tag{2.53}$$

where N_j is the number of atoms in shell j, at distance R_j from the central atom, and σ_T is the total scattering cross-section, including elastic and inelastic effects.

The probability of reaching a given shell without scattering is given by the product of the transmission functions for the intermediate shells. The attenuation coefficient is then

$$A_j(k) = \prod_{p=1}^{j-1} T_p , \tag{2.54}$$

where $A_1(k) = 1$. Note that A is, in general, energy dependent.

For the purpose of this thesis the simpler expression of Sayers et al. is used. Sayers et al. also use a factor $e^{-2k^2\sigma^2(T)}$ to account for the thermal motion of the atoms, where σ^2 is the (temperature-dependent) mean square relative displacement of an atom about its average distance from the central atom. This factor will be discussed further in the next section. Accounting for attenuation and thermal effects, Eqn. 2.52 becomes

$$\chi(k) = \frac{1}{k} \sum_{\beta \neq \alpha} |f_\beta(\pi)| \frac{e^{-2R_{\alpha\beta}/\lambda}}{R_{\alpha\beta}^2} e^{-2k^2\sigma^2_\beta(T)} \sin(2kR_{\alpha\beta}+2\eta_1+\theta_\beta). \quad (2.55)$$

Eqn. 2.55 is the basic formula for the EXAFS.

Section 2.5 - Radial Structure Function

Working with a formula similar to Eqn. 2.55 based on their point-scattering theory, Sayers et al. (1971) showed how the experimental data may be inverted to obtain a radial structure function $\phi(r)$. With

$$\chi(k) = -\frac{f(k)}{k} \sum_j \frac{N_j e^{-\gamma r_j}}{r_j^2} e^{-\frac{1}{2}\sigma^2_j k^2} \sin(2kr_j+2\eta(k)), \quad (2.56)$$

they take the Fourier transform

$$\begin{aligned}
\phi(r) &= -\sqrt{2/\pi} \int_0^\infty \frac{k\chi(k)}{f(k)} \sin(2kr+2\eta(k))dk \\
&= \frac{1}{2} \sum_j \left(\frac{N_j e^{-\gamma r_j}}{r_j^2 \sigma_j}\right) e^{-2(r-r_j)^2/\sigma_j^2} . \quad (2.57)
\end{aligned}$$

The sum is taken over shells j. A Fourier transform of the experimental data yields a function which represents a series of normal gaussian functions centered at each shell radius.

Here it is seen that the use of the disorder term $e^{-2k^2\sigma^2}$ is based on the assumption that the real-space distribution function is gaussian.

Eisenberger and Brown (1978) have recently discussed the consequences of non-gaussian distributions. They show that if the distribution has asymmetric components with respect to $\overline{R}_{\alpha\beta}$, an additional phase will be introduced into the sine function of Eqn. 2.55. No real distribution is purely gaussian so that this has implications for the analysis of experimental data.

One more point needs to be mentioned here. Experimental data represents an averaging over many atoms. In an amorphous material, the environment of each atom is unique and, therefore, the averaging procedure makes an additional contribution to the probability distribution that is structural in origin. If this is also assumed to be gaussian, then there is a term $e^{-2k^2\sigma_s^2}$ implicit in Eqn. 2.55, where σ_s^2 is the structural contribution to the disorder. As discussed above, if this distribution is asymmetric an additional phase will be introduced into Eqn. 2.55.

In actual practice (Stern et al., 1975) the transform taken is

$$\phi_n(r) = \frac{1}{2\pi} \int_{k_{min}}^{k_{max}} k^n \chi(k) e^{2ikr} \, dk , \qquad (2.58)$$

where n = 1 or 3. Stern (1974) has related the n = 1 transform to the spatial variation of a scattering matrix and the n = 3 transform to a pseudocharge density. Stern et al. claim the most satisfactory results with n = 3. There are two reasons for this. On the one hand n = 3 preferentially weights the high-energy part of the absorption spectrum where Eqn. 2.55 is a better approximation. Secondly, there is a difficulty in defining

precisely at what energy with respect to the edge the origin of k should be located. This uncertainty affects most the low-energy part of the spectrum. The n = 3 transform de-emphasizes this uncertainty and is much less sensitive to the choice of k_{min}.

There is an additional reason for choosing to do the above transform. Lee and Beni (1977) have shown that, provided the real space distribution is gaussian, the real part of the transform passes through zero at the peak position. Thus the magnitude peaks at the same position as the imaginary part. This assumes that the location of k = 0 is known. The point made by Lee and Beni is that a priori knowledge of the complex phase shifts enables one to determine k = 0 by comparing the magnitude with the imaginary part of the transform. Taking the magnitude of a complex transform also has a smoothing effect, which becomes important if the k-space range is narrow.

The function $\phi_n(r)$ contains information on the number, distance to and distribution of atoms surrounding the absorbing atom. Stern et al. (1975) have discussed in detail how to extract such information using the Fourier transform technique. They also show how to extract such parameters as the electron scattering amplitudes, mean free paths, disorder terms and phase shifts.

Section 2.6 - Summary

Using Green's functions and the T-matrix formalism, the normalized oscillatory part of the X-ray absorption spectrum was calculated (Eqn. 2.43). The one-electron approximation was used and it was assumed that the potentials of the atoms could be modeled by muffin tins. It was further assumed

that relaxation effects could be ignored and that the absorbing atom could be represented by a screened core hole. Eqn. 2.43 is the starting point for a multiple scattering treatment of the problem.

An analytic expression was then derived in the high-energy approximation (Eqn. 2.52). Accounting for attenuation and thermal effects led to the basic formula for the EXAFS, Eqn. 2.55.

The Eqns. 2.43 and 2.55, along with the Fourier transform, Eqn. 2.58, are the primary tools we will employ in this investigation.

Chapter 3 - Structure of Amorphous Materials

In this chapter we consider the structure of amorphous materials. In section 3.1 we present a general description of the amorphous state and introduce the structural model. In section 3.2 we deal with the particular case of the continuous-random-network models for amorphous semiconductors, while we treat the dense-random-packing-of-hard-spheres models for metallic glasses in section 3.3.

Section 3.1 - The Amorphous State

To describe the amorphous state we begin with the concept of a disordered system. Two general classes of disordered systems are encountered in solid state physics. On the one hand we may have a periodic array of atoms of different types, the different types being randomly distributed throughout the lattice. We shall call this "substitutional" disorder. On the other hand we may have an array of identical atoms which are not periodically positioned. This latter class of "positionally" disordered systems provides a model for amorphous solids. If a positionally disordered system has everywhere the same coordination of nearest neighbors we say that it is "topologically" disordered. This classification scheme is illustrated in Figure 3.1. In general, of course, most real amorphous materials are both substitutionally and positionally disordered, since they contain atoms of more than one kind.

A crystalline structure is specified by the few relative coordinates of the atoms comprising the unit cell. These coordinates are accessible through X-ray diffraction experiments. Such a characterization of an
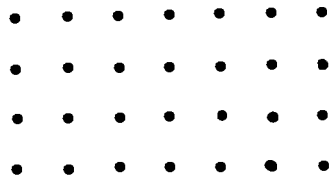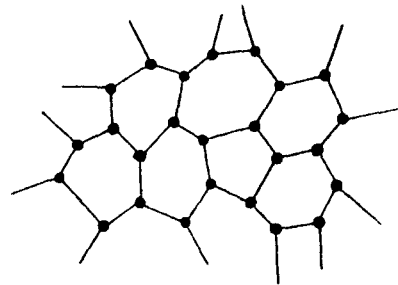
(a)
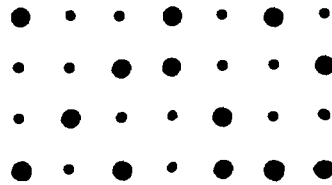
(b)
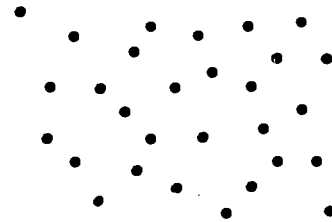
(c)

(d)

Figure 3.1

Various types of disorder encountered in
solid state physics: (a) perfect order;
(b) substitutional disorder; (c) positional
disorder; (d) topological disorder.
[After Weaire and Thorpe (1971).]

amorphous system is neither convenient nor accessible. A description
which is useful and accessible (X-ray, neutron and electron scattering
experiments) is given in terms of an average radial density function.[1]

The average radial density function (ARDF) is the number of atoms
at distances between r and r + dr from some atom chosen as origin averaged
over the surface of a sphere ($4\pi r^2$), further averaged by taking each atom
in turn as the origin. In a system where more than one atomic species
is present the ARDF can be thought of as a linear combination of density
functions centered about atoms of a single type. (Recall from Chapter 2
that this is the type of density function that is available via analysis
of the EXAFS.) It is the composite ARDF that is accessible through conven-
tional diffraction experiments.

One approach to the understanding of amorphous structure has been to
create structural models which will reproduce such experimentally accessible
features of a system as the ARDF or its vibrational spectrum. It is clear
that the binding forces between atoms in a solid should be similar whether
the structure is crystalline or amorphous. Thus, even in the amorphous case,
short-range order (SRO) over a distance of a few atomic radii will generally
be present. This suggests that a useful characterization of an amorphous
solid might be provided by the coordinates of a few hundred
or a few thousand atoms. Much research has been devoted to developing such
models.

Two general classes of models for amorphous solids may be distinguished.
The microcrystalline models are those in which most of the atoms are
arranged in small microcrystals which are randomly oriented with respect
to each other. Thus these models feature abrupt structural discontinuities.

This approach has not, in general, met with much success and we will not consider these models further.

The other models are those in which the individual atoms are arranged in a continuous random way without the abrupt discontinuities of the microcrystalline models. These are of two types; the continuous-random-network (CRN) models for amorphous semiconductors, and the dense-random-packing-of-hard-spheres (DRPHS) models for metallic glasses. The former are suitable for small coordination numbers (2,3,4) while the latter are appropriate for the higher coordination numbers found in metallic systems.

Section 3.2 - Continuous-Random-Network (CRN) Models

Zachariansen(1932) first proposed the concept of a non-periodic random network as a general model for glasses. The first quantitative success of this model was obtained by Bell and Dean (1966). Their ball-and-stick model of SiO_4 tetrahedra, arranged according to certain rules, yielded distribution functions in agreement with experiment.

The most extensive modelling using the CRN concept has been for the amorphous tetrahedrally-coordinated semiconductors Si and Ge. In these models each atom has four neighbors in an approximately tetrahedral arrangement (topological disorder). Variation in the tetrahedral angle and relative rotation of adjoining tetrahedra lead to non-crystallinity.

The first of these models was hand-built by Polk (1971) and consisted of 440 atoms. (Comparison of this model with experiment is shown in Figure 3.2.) This structure was later enlarged to 519 atoms (Polk and Boudreaux, 1973) to increase the size of the cluster and make it more nearly spherical. The coordinates of the atoms were measured by an accurately

Figure 3.2

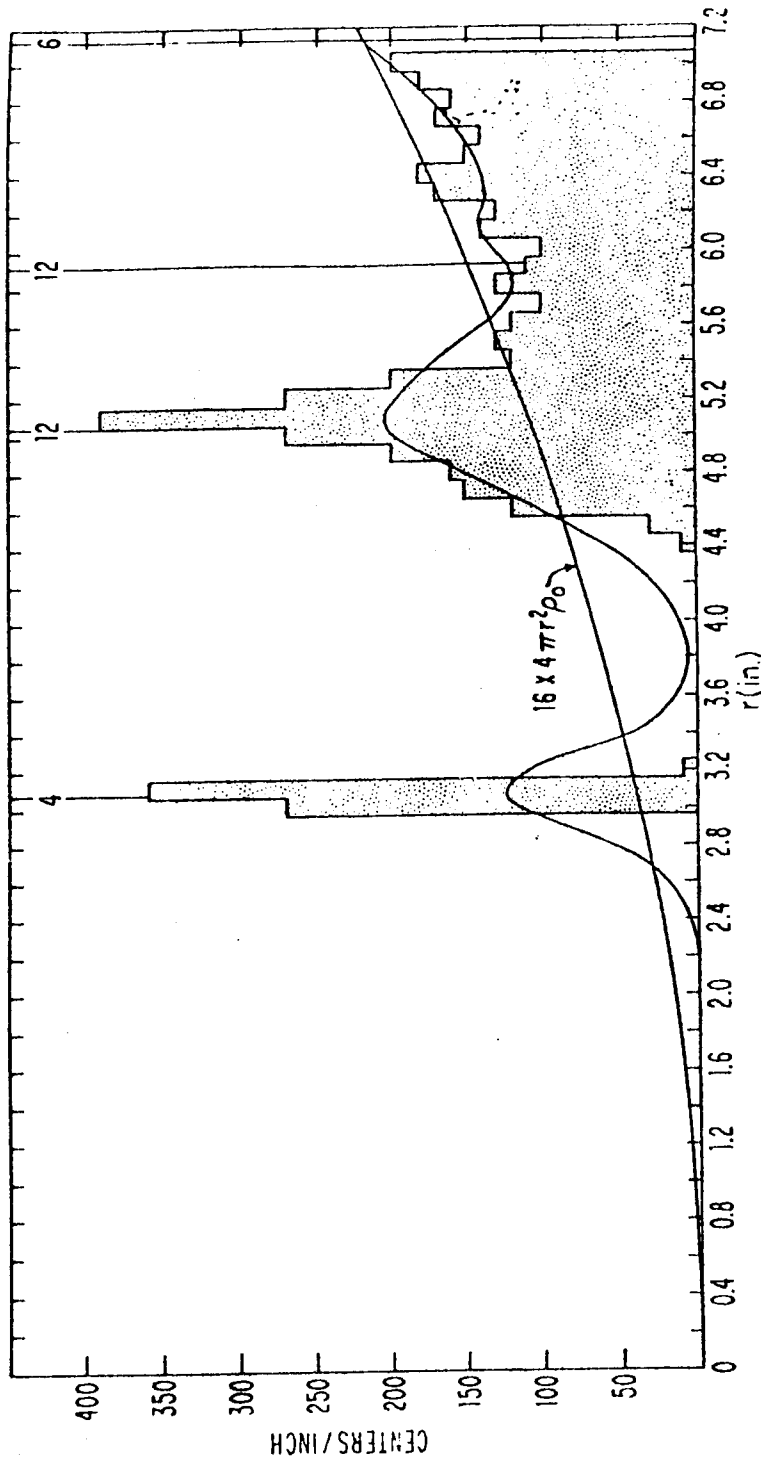Comparison of the ARDF for the random-network model of Polk (1971) (histogram) with experimental data from electron diffraction by amorphous Si by Moss and Graszyk (1969). The parabola represents the average density and the vertical lines and corresponding numbers represent the position and number of neighbours in a crystal with a nearest-neighbour separation equal to the mean separation in the model. [After Paul (1976).]

positioned laser beam. Computer techniques were then used to determine new coordinates which would reduce the variation in bond lengths (distances between nearest neighbors) to nearly zero. The ARDF of this structure is in good agreement with experiments.

The refinement of this 519-atom model has been taken a stage further by Steinhardt et al. (1973). The atom positions were systematically adjusted so as to minimize the Keating (1966) expression for the elastic energy of a tetrahedrally-bonded solid in terms of the bond lengths d and bond angles:

$$V = \frac{3}{16} \frac{\alpha}{d^2} \sum_{\ell,i} (r_{\ell i} \cdot r_{\ell i} - d^2)^2 + \frac{3}{8} \frac{\beta}{d^2} \sum_{\ell(i,i')} (r_{\ell i} \cdot r_{\ell i'} + \frac{1}{3} d^2)^2$$

$$(3.1)$$

Here α and β are bond-stretching and bond-bending force constants where β/α was taken as 0.2, which is in a range of plausible values indicated by phonon frequencies for diamond cubic Si and Ge. The first sum is over all atoms ℓ and their four neighbors i; the second sum is over all atoms and pairs of neighbors; $r_{\ell i}$ is the vector from ℓ to its ith neighbor. This model is referred to as being "fully relaxed", the relaxation procedure accounting for a nearly 40% decrease in the total stored energy in the unrelaxed model due to a decrease in the rms angular deviation.

These "Polk-type" models are generally consistent with X-ray diffraction data. They have also been used to obtain the vibrational density of states and the Raman and infrared spectra of Si and Ge. These results compare favorably with experimental measurements (Alben et al., 1975). It is the fully-relaxed Polk model that we explore further in Chapter 4 as a model for amorphous Ge.

It remains to be pointed out that since Polk's original model, CRN models have been built solely by computer techniques (for example, Shevchik and Paul, 1972). Refinement of these models is an active field of research.

Section 3.3 - Dense-Random-Packing-of-Hard-Spheres (DRPHS) Models

The DRPHS was first proposed by Bernal (1959), as a model for liquids. (The spheres are considered dense in the sense that the structure contains no internal holes large enough to accommodate another sphere.) It was Cohen and Turnbull (1964) who suggested that the model was appropriate for a monatomic glass.

The first DRPHS models were built by kneading and squeezing a bladder filled with ball bearings. The most ambitious such effort was the 8000-ball-bearing cluster of Finney (1970). Cargill (1970) has pointed out that the agreement between the structure of this model and X-ray results from amorphous Ni-P alloys is remarkable (Figure 3.3).

The first computer-generated DRPHS was constructed for single-size spheres by Bennett (1972). Bennett-type structures are generated by starting with a small seed cluster. The cluster is examined to determine all possible sites for which an added sphere would be in hard contact with three spheres already in the cluster. Then a site is chosen according to some criterion. Bennett investigated a "global" criterion by which the new atom was added at the site closest to the center of the original cluster, and a "local" criterion by which the new atom was added at the site having the least distance from the plane of its three neighbors. These computer-generated clusters are similar in many ways to those built with ball-bearings.
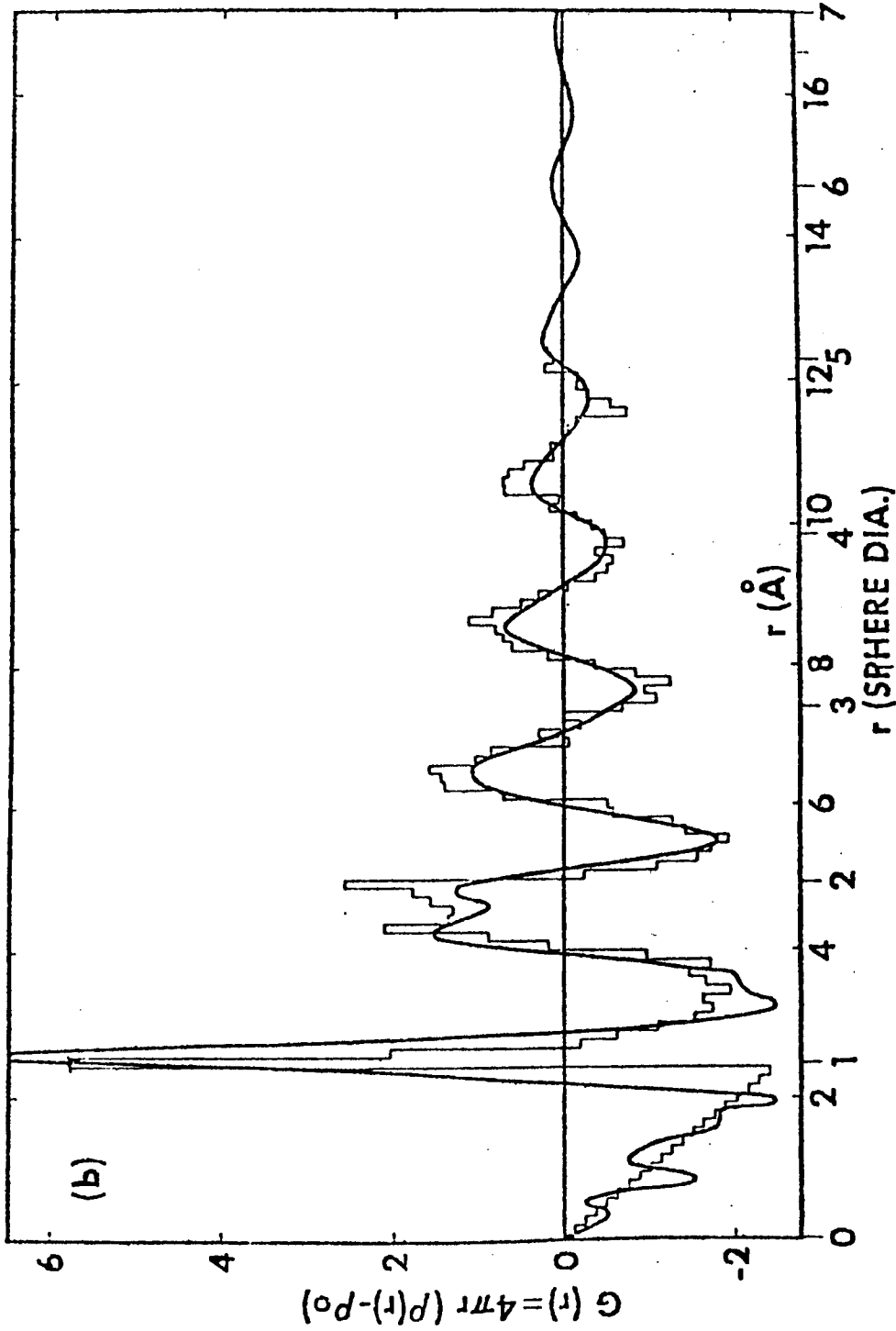
Figure 3.3

Comparison of reduced radial distribution functions $G(r)$ for Finney's DRPHS structure and for amorphous $Ni_{76}P_{24}$. [After Cargill (1970).]

As mentioned above, a single-size DRPHS has been shown to agree favorably with data obtained on Ni-P alloys. (The diameters of Ni and P differ by less than 3%.) In Chapter 5 we use a computer-generated single-size DRPHS as a model for amorphous Ni-P.

The model has subsequently been generalized (Polk, 1973) to include spheres of two different sizes for binary metal-metal alloys where the components differ significantly in size. We conclude by pointing out that the DRPHS model has been used to investigate the equilibrium density, binding energy, and elastic constants of amorphous metals (Weaire et al., 1971), the vibrational spectrum of a metallic glass (Heimendahl and Thorpe, 1975), and the magnetic properties and Mössbauer absorption spectra of amorphous metallic alloys of rare earths and transition metals (Cochrane et al., 1974).

Chapter 4 - Analysis of a CRN Model

In this chapter we apply the EXAFS formalism to the 519-atom, fully-relaxed, tetrahedrally-coordinated, continuous-random-network (CRN) structure discussed in Chapter 3. We use the particular case of germanium with a bond length of 2.45Å. We have two reasons for doing this. First of all, a model calculation of the EXAFS allows us to explore the usefulness of the EXAFS as a technique for structural investigation in an ideal way. We shall have no experimental noise nor temperature effects to worry about. Nor need we be concerned about many-body effects or other problems which invalidate the theory near the absorption edge. Secondly, as discussed in Chapter 3, model building is a useful way of exploring atomic structure. We hope to shed some light on the usefulness of the EXAFS as a means of choosing between competing structural models.

In Section 4.1 we look at the model in some detail by generating a histogram of the average radial density function. The EXAFS function CHI is calculated and discussed in Section 4.2. In Section 4.3 radial density functions are generated by the Fourier Transform technique. Some limitations on this technique are discussed. We use this technique to obtain information about the disorder of the nearest neighbor distribution in Section 4.4. In Section 4.5 some recent experimental data is presented and discussed. Section 4.6 contains a summary and some conclusions.

Section 4.1 - Analysis of the Model

A histogram of the average radial density function (ARDF) is constructed as follows: count the number of atoms at distances between r and $r + \Delta r$ from some atom chosen as origin. Average this by taking each

atom in turn as origin. Divide by $4\pi r^2$ to obtain the average radial density.

GE (for convenience we give the model a name) is approximately spherical and contains 519 atoms. Those on the surface have less than four nearest neighbors; i.e. dangling bonds exist. Some care must be taken to ensure that these surface atoms do not "contaminate" the calculations. We wish to examine the density function as far as $r \approx 7.5\overset{o}{A}$ (3 bond lengths). This means that we must have a $7.5\overset{o}{A}$ "sphere" of atoms surrounding each of the atoms over which we wish to average. In this case "contamination" is expected to be minimal and will certainly not affect the statistics on the first few nearest neighbors. This condition limits us to a central group of 80 atoms.

To construct the histogram we chose $\Delta r = \frac{1}{40}$ th of a bond length. In order to investigate possible size effects histograms were constructed with 10, 20 and 40-atom central groups as well as with 80. The results for the 40 and 80-atom averages are shown in Figure 4.1.

Before discussing these histograms we present some additional data on GE which were calculated from the known atomic positions. Table 4.1 gives the mean positions and mean square deviations, σ^2, of the first and second nearest neighbor distributions, averaged over 10, 20, 40 and 80 atoms.

The most outstanding feature of the histograms (Figure 4.1) is the very sharp, isolated peak representing the nearest neighbor distribution. A smaller broader peak at about $4\overset{o}{A}$ indicates a fairly well-defined second neighbor distribution. Beyond this the features become less distinct.

The most notable difference between the two histograms is the sharpening of the peaks at $4.0\overset{o}{A}$ and $4.8\overset{o}{A}$ when 80 atoms are used. But the general
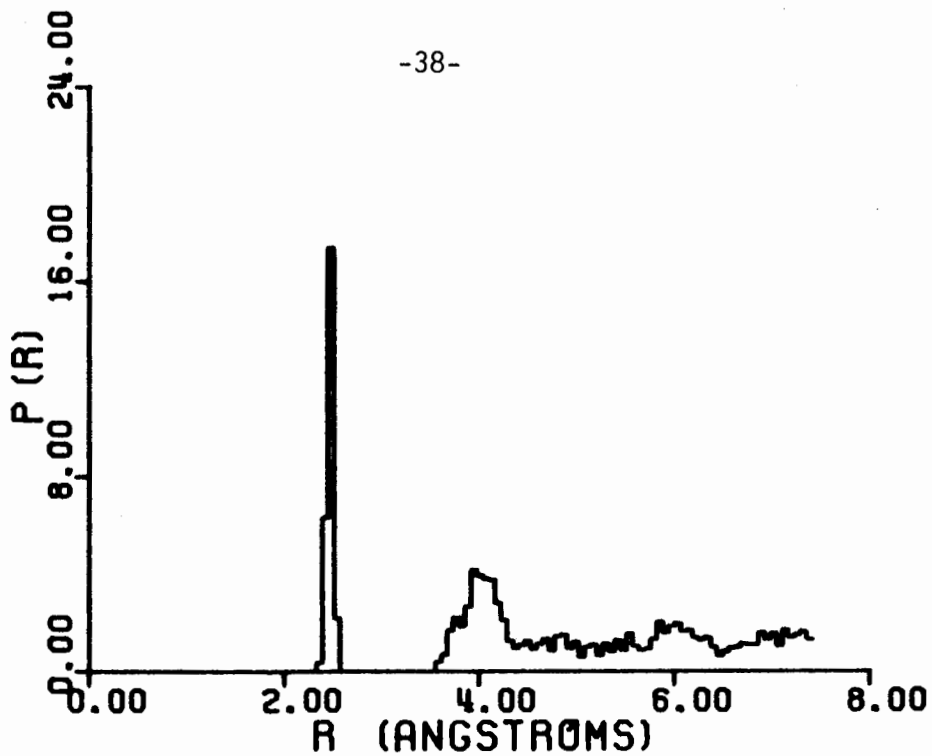
Figure 4.1a.   ARDF for GE averaged over 40 atoms.
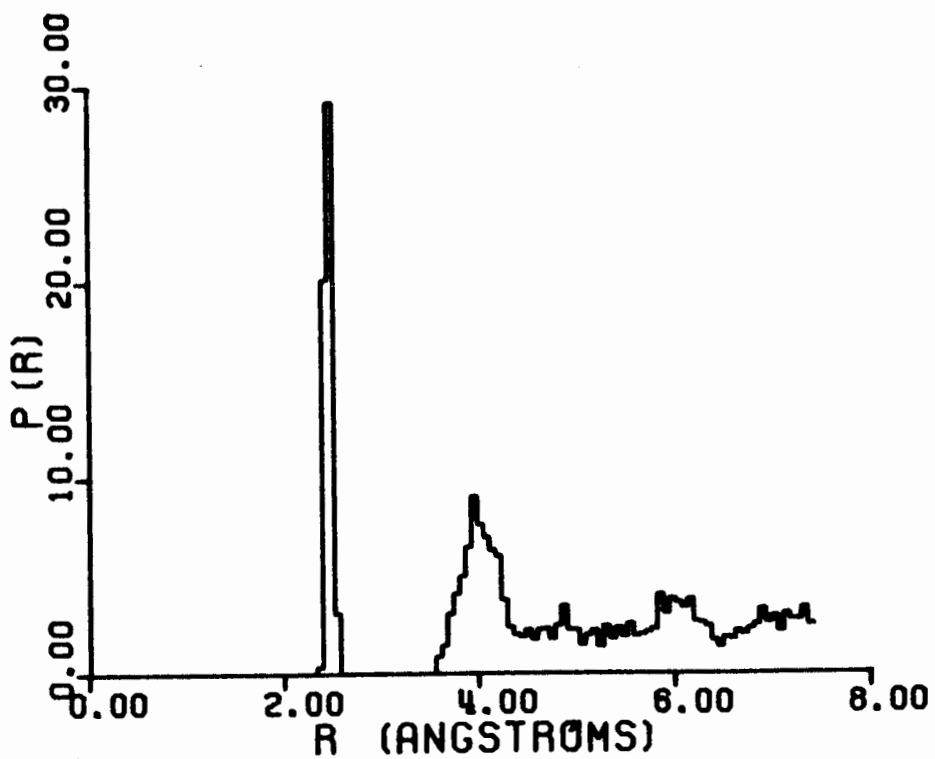
Figure 4.1b.   ARDF for GE averaged over 80 atoms.

Table 4.1

Data on GE

Central Atoms	10	20	40	80
$\overline{R}_1(\overset{\circ}{A})$	2.47	2.47	2.47	2.46
$\sigma_1^2(\overset{\circ}{A}{}^2)$	.00097	.00105	.00088	.00093
$\overline{R}_2(\overset{\circ}{A})$	4.02	4.03	4.02	4.01
$\sigma_2^2(\overset{\circ}{A}{}^2)$	.03934	.03915	.03547	.03397

features (peak positions and relative heights) are quite similar. Table 4.1 shows some fluctuations in σ_1^2, but a monatonic decrease in σ_2^2, as the number of central atoms increases. We can draw no conclusions from this. However, we are confident that enlarging the structure would not significantly alter the general features of Figure 4.1b.

Section 4.2 - Calculation of the EXAFS

We now calculate the EXAFS function CHI for GE via Eqn. 2.55. Since the atoms are all of the same atomic species the magnitude of the backscattering amplitude, $T(k)$, may be taken out of the sum. We set $\sigma^2(T) = 0$ indicating that the system is taken to be at $0°K$. Then we have

$$\chi(k) = \frac{T(k)}{k} \sum_j \frac{e^{-2R_j/\lambda}}{R_j^2} \sin(2kR_j + \delta_j(k)), \qquad (4.1)$$

where we have written

$$\delta_j(k) = 2\eta_1(k) + \upsilon_j(k). \qquad (4.2)$$

The sum is over all atoms within 7.5Å of the central atom.

A constant value of $\lambda = 4.6$Å was used for the mean free path of the photoelectron (Stern et al., 1975). A linear form was used for the phase shift (Ashley and Doniach, 1975),

$$\delta(k) = 4.5 - 0.41k. \qquad (4.3)$$

The magnitude of the backscattering amplitude has been calculated

(Teo et al., 1977) and fitted to the form

$$T(k) = \frac{A}{1 + B^2(k-C)^2} , $$ (4.4)

with A = 0.601, B = 0.1716 and C = 8.230 for germanium. The parameters in Eqns. 4.3 and 4.4 requre k to be expressed in $\overset{o}{A}^{-1}$.

Figure 4.2 shows CHI (weighted with k because of the 1/k divergence at low k) averaged over 80 atoms. Figure 4.3 is the nearest-neighbor-only contribution to k-CHI. There are two interesting features of these plots which we would like to point out. First, from Eqns. 4.1 and 4.4 we expect to see an oscillatory function with a Lorentzian envelope peaked at $8.230\overset{o}{A}^{-1}$. In fact the envelope of Figure 4.2 is obviously not Lorentzian and both figures show peaks at $k < 8\overset{o}{A}^{-1}$. This shift in the peak position is explained by the averaging procedure. As discussed in Chapter 2, since the environment of each atom is different, the averaging procedure intro- duces an implicit damping term, $e^{-2k^2\sigma^2}$, into Eqn. 4.1 due to the structural disorder of the system. This shifts the peak position towards lower k.

The other interesting point to notice is the similarity between Figures 4.2 and 4.3. For $k \gtrsim 8\overset{o}{A}^{-1}$ the two functions are virtually identical, major differences occurring only for $k \lesssim 5\overset{o}{A}^{-1}$. This obviously means that at sufficiently high energy only the nearest neighbors contribute to the EXAFS. This point is further illustrated by Figure 4.4 which shows the second neighbor contribution. Notice that this contribution is quite small above $5\overset{o}{A}^{-1}$. Reference to Table 4.1 indicates why this might be expected. The disorder (σ^2) of the second neighbor distribution is much greater than that of the first. Thus the second neighbor oscillations are damped out much more quickly. Second neighbor effects are further reduced
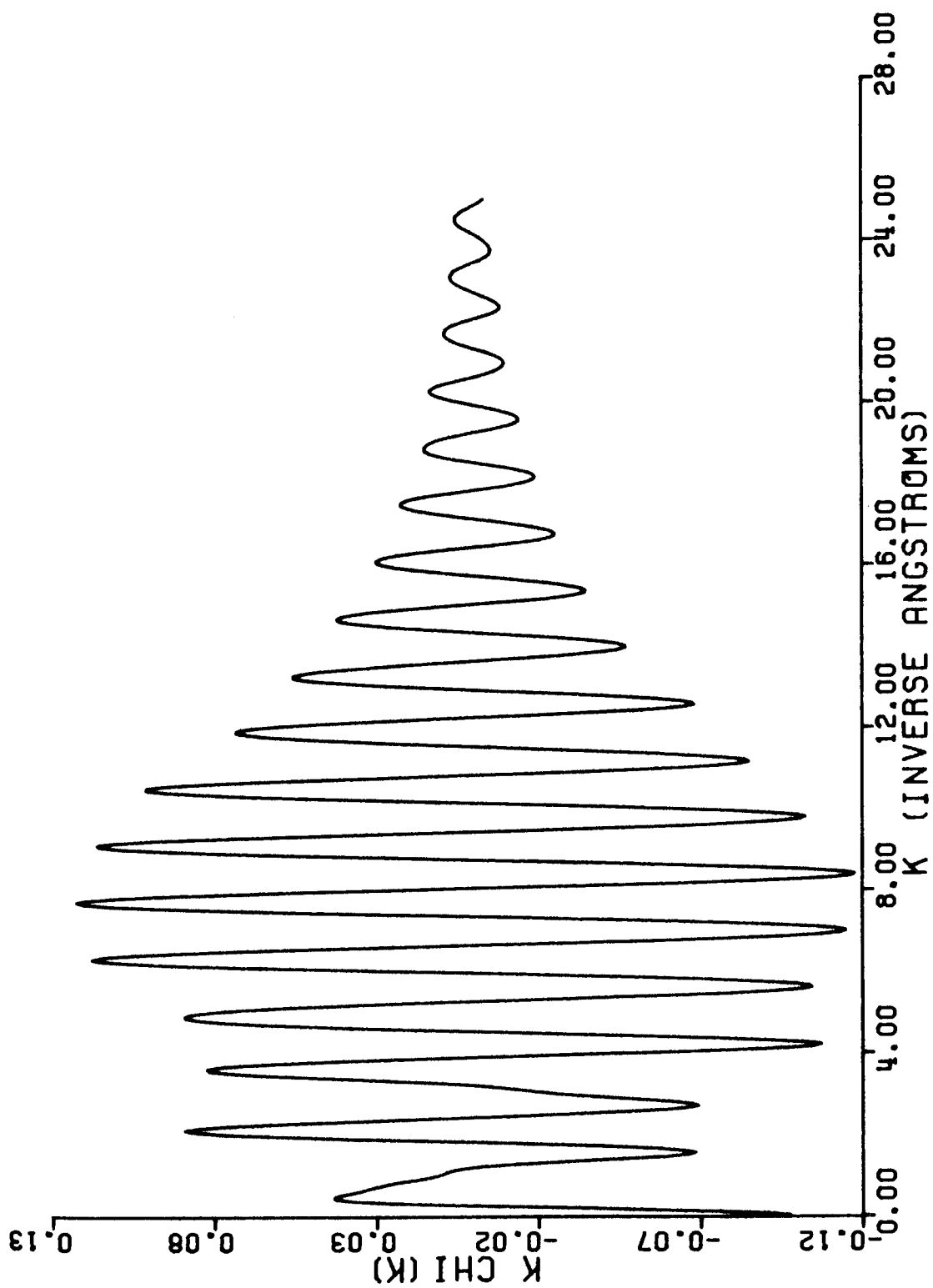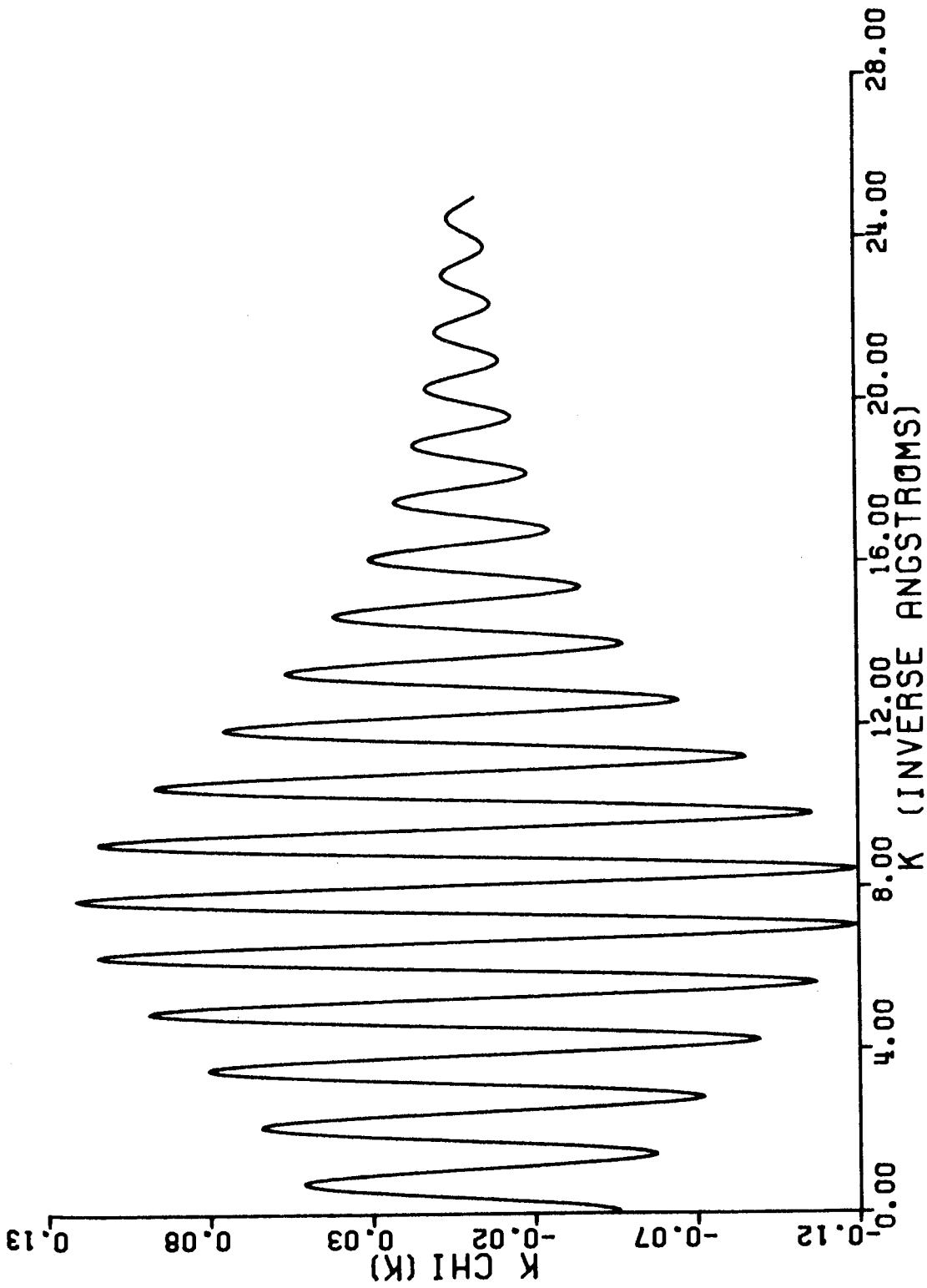
Figure 4.2. K x CHI for GE.

-43-

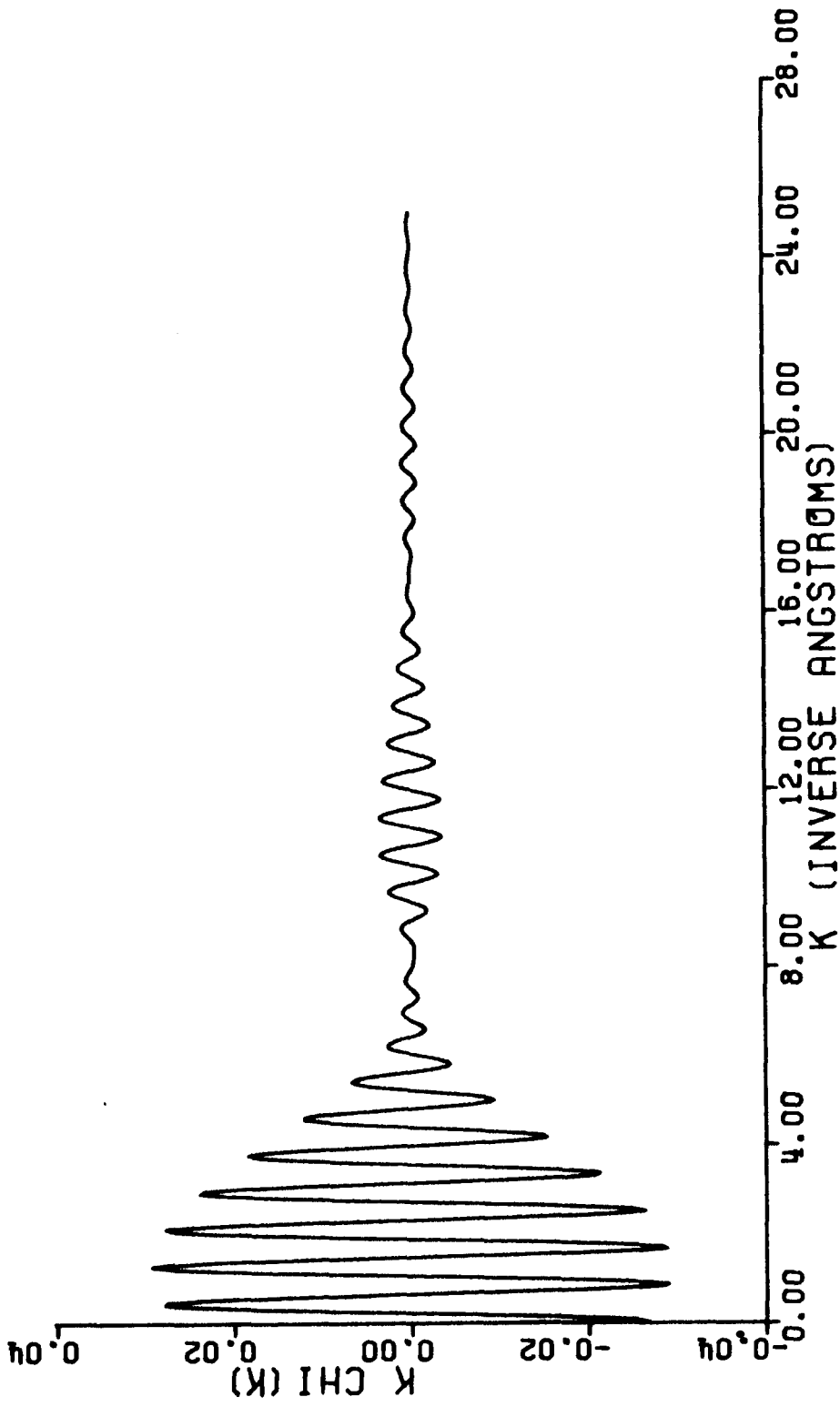Figure 4.3. Nearest neighbor contribution to K x CHI for GE.

Figure 4.4. Second neighbor contribution to K x CHI for GE.

by the attenuation term $e^{-2R/\lambda}$. Thus, even below $5\overset{\circ}{A}^{-1}$, the second neighbor oscillations have considerably less amplitude then those due to the first neighbor distribution.

We pause here to emphasize the point made in the preceding paragraph. EXAFS is a tool for the investigation of atomic structure. To gain useful information about structure beyond the nearest neighbors it is necessary to have, and be able to interpret, low k information. But, as previously discussed, the assumptions which went into the development of the EXAFS formalism are not valid for sufficiently low energies. This point has implications for the investigation of models. If competing models differ significantly only beyond the nearest neighbor distribution, lack of low k information may make it impossible to distinguish between such models with the EXAFS technique. We shall have occasion to consider this further.

Section 4.3 - Fourier Transform Analysis, Part I

As discussed in Chapter 2 the magnitude of a Fourier transform of the EXAFS function CHI yields a radial density function for the structure involved. The transform taken is

$$\phi_n(r) = \frac{1}{\sqrt{2\pi}} \int_{k_{min}}^{k_{max}} k^n \chi(k)e^{2ikr} \, dk, \tag{4.5}$$

where $n = 1$ or 3.

A Fourier transform is an integral from 0 to ∞. Integrating over a finite range means that the integrand has been convoluted with a "window" function, one which takes the value 1 over the desired integration range and 0 elsewhere. The effects of this are easy to analyze:

$$\left| \int_{k_{min}}^{k_{max}} dk \; e^{2ikr} \right| = \left| \frac{\sin[(k_{max}-k_{min})r]}{r} \right| . \tag{4.6}$$

This function has the periodicity

$$\Delta r = \frac{\pi}{k_{max}-k_{min}} . \tag{4.7}$$

Figure 4.5 shows how this affects a transform. This is the $n = 1$ transform of the nearest neighbor contribution to CHI over the range .375-24.125Å^{-1}. (All transforms discussed in this paper were taken with k_{min} and k_{max} being chosen as points where CHI ≈ 0 and such that an integral number of oscillations of the function were included.) We expect to see a fairly sharp peak at the nearest neighbor distance of 2.45Å, shifted by -.205Å because of the linear phase shift of Eqn. 4.3. We do in fact see this (the peak is located at 2.25Å). But the peak is accompanied by a series of periodic oscillations decreasing in amplitude away from the peak. These oscillations are due to the finite transform. Eqn. 4.7 predicts a periodicity $\Delta r = .13$Å, and this is what is observed.

Transforms were taken of the full function CHI over the range .275-24.125Å^{-1} for both $n = 1$ and $n = 3$. These are shown in Figure 4.6. There are two important things to notice here. Both figures show a strong peak at $r = 2.25$Å as expected. However, the k and k^3 weightings have markedly different effects for $r \gtrsim 3$Å. As pointed out in Section 4.2, information about structure beyond the nearest neighbor distribution is contained in the low k region of the EXAFS. Weighting with k^3 de-emphasizes this part of the spectrum more than weighting with k. Hence, as seen in Figure 4.6b, this results in less information about the structure at larger r.
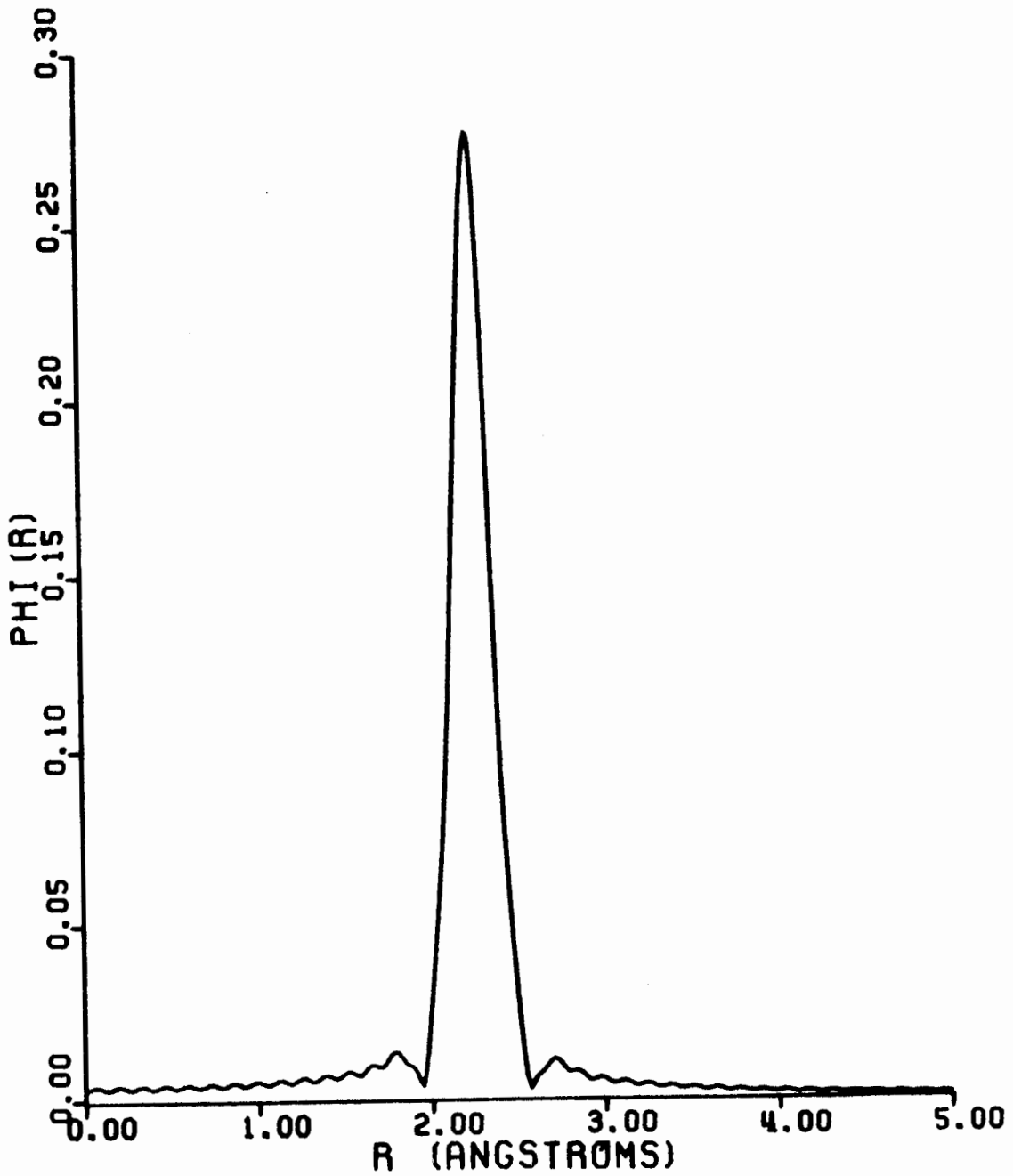
Figure 4.5. Fourier transform (n = 1) of the nearest neighbor contribution to the EXAFS over the range .375 - 24.125$Å^{-1}$.
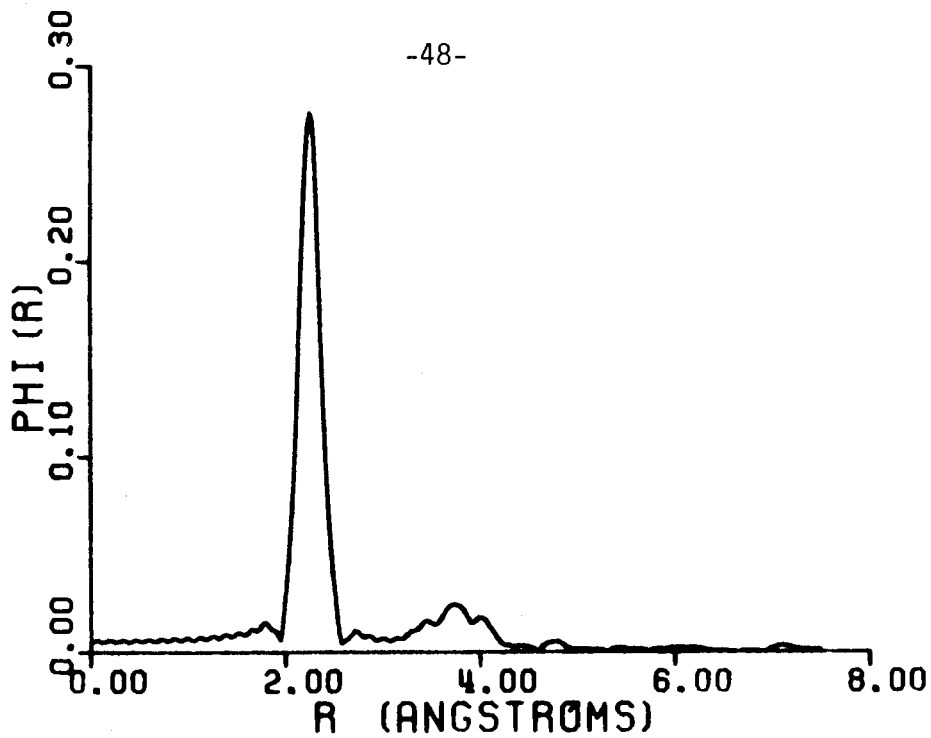
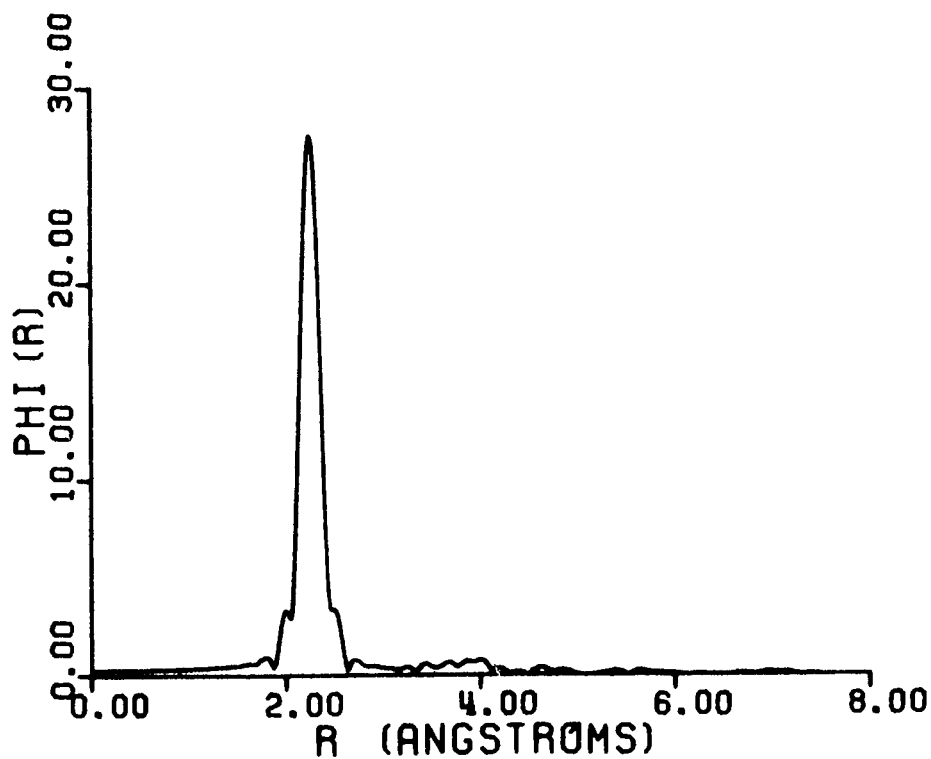Figure 4.6a. N = 1 transform of CHI from .275 – 24.125$\overset{\circ}{A}^{-1}$.

Figure 4.6b. N = 3 transform of CHI from .275 – 24.125$\overset{\circ}{A}^{-1}$.

This point is made very clear in Figure 4.7 where the transform of Figure 4.6a is compared with the histogram of Figure 4.1b. The transform has been shifted by +.205 to cancel the effect of the linear phase shift. Clearly the second peak of the $n = 1$ transform corresponds very well with the second peak of the histogram. However, Figure 4.6b shows that the $n = 3$ transform washes out most of this information. In fact, the position of the second peak in the $n = 1$ transform corresponds to a minimum in the $n = 3$ transform!

Clearly $n = 1$ is to be preferred over $n = 3$. Because of the uncertainty in the location of $k = 0$, $n = 3$ is preferred in the analysis of experimental data (Stern et al., 1975). This is less sensitive to the choice of k_{min} than $n = 1$. But the procedure yields less information.

We note that the second peak of the $n = 1$ transform occurs at $r = 3.73\text{Å}$. The corresponding peak of the histogram is centered at $r = 3.95\text{Å}$, the width being $.06\text{Å}$. Because of the nature of histograms there is some ambiguity in the shift of the "peak" position. The distribution is asymmetric and there may be a shift due to this asymmetry. Eisenberger and Brown (1978) state that if $\sigma^2/\overline{R}$ and $\sigma^2/\lambda < .01\text{Å}$ then the effects of the asymmetry are negligible. This is the case here (see Table 4.1).

It is of iterest to look at the $n = 1$ transform to determine the effects of varying k_{min} and k_{max}. A number of transforms were taken over various ranges. Some of these are shown in Figures 4.8 - 4.10.

There is no need to comment on these figures in detail. They all show the characteristic oscillations, with periodicity given by Eqn. 4.7, which are artifacts of the finite-range transform. Notice that reducing
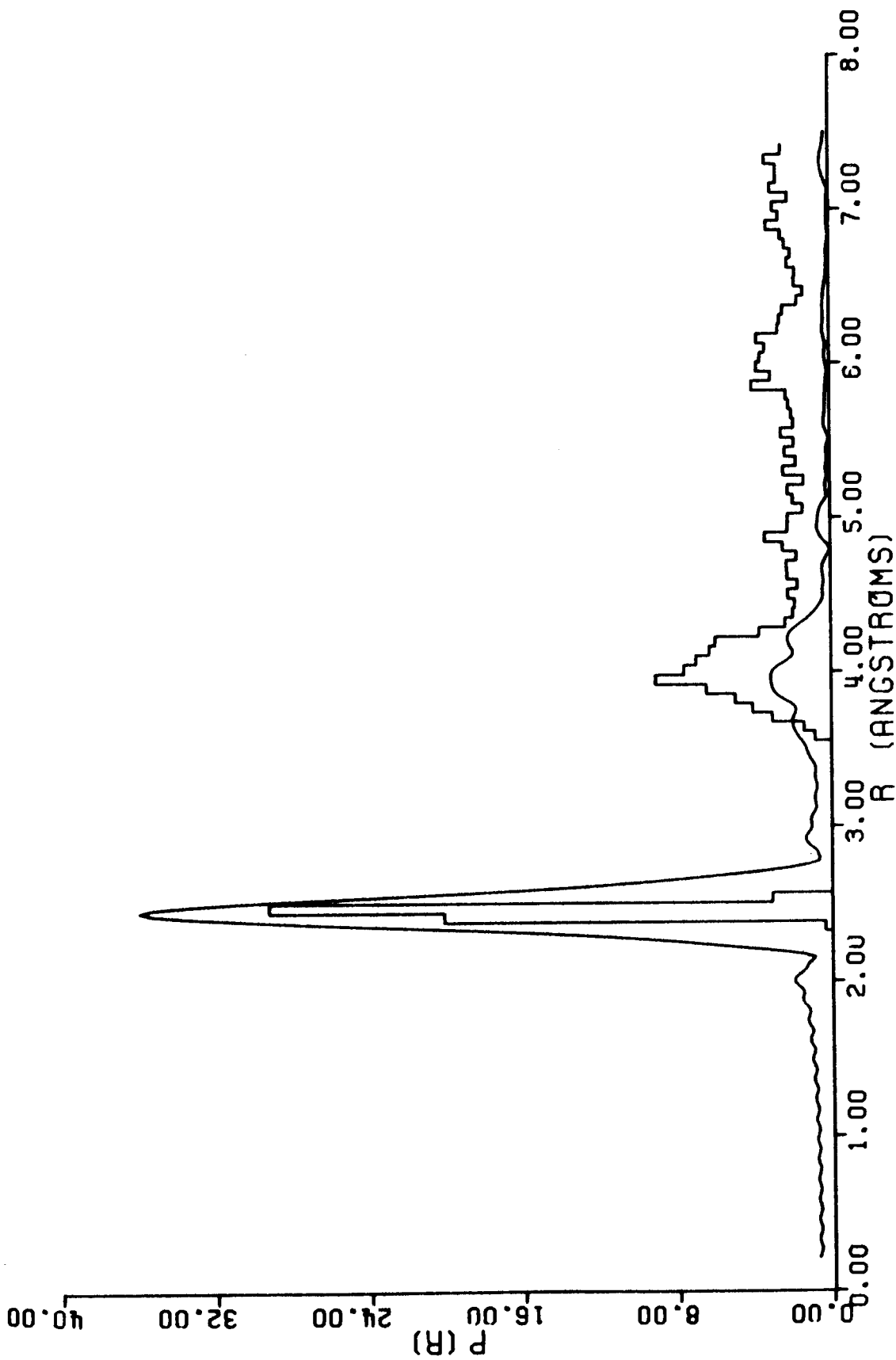
Fig 4.7. Comparison of the Fourier (n = 1) transform of CHI with the histogram of the ARDF.
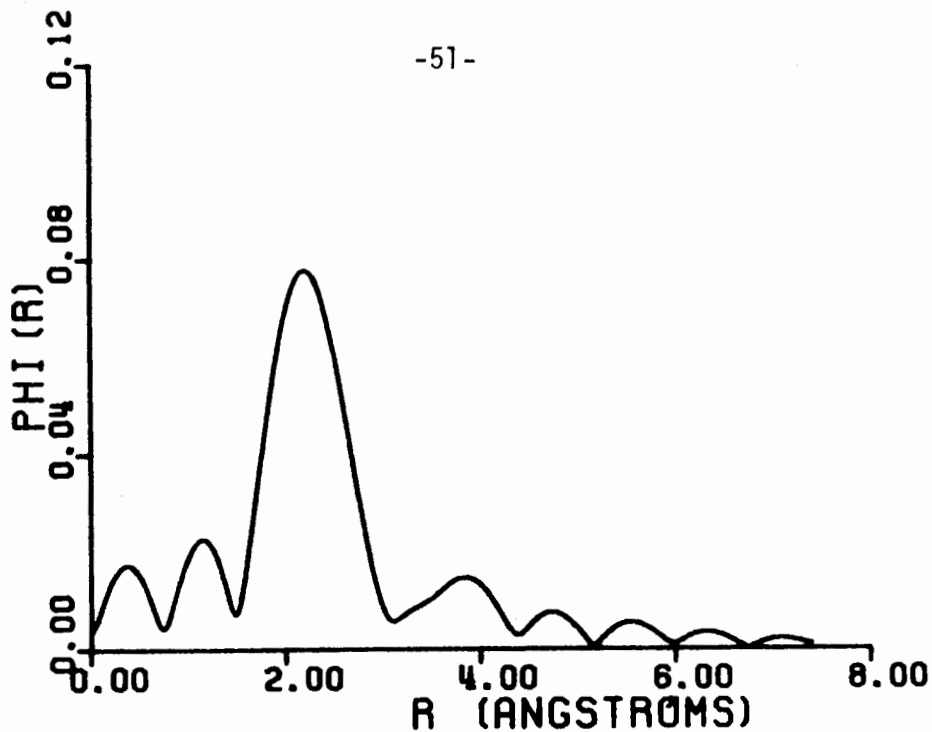
Figure 4.8a.   N = 1 transform of CHI from $1.825 - 7.375Å^{\circ-1}$.
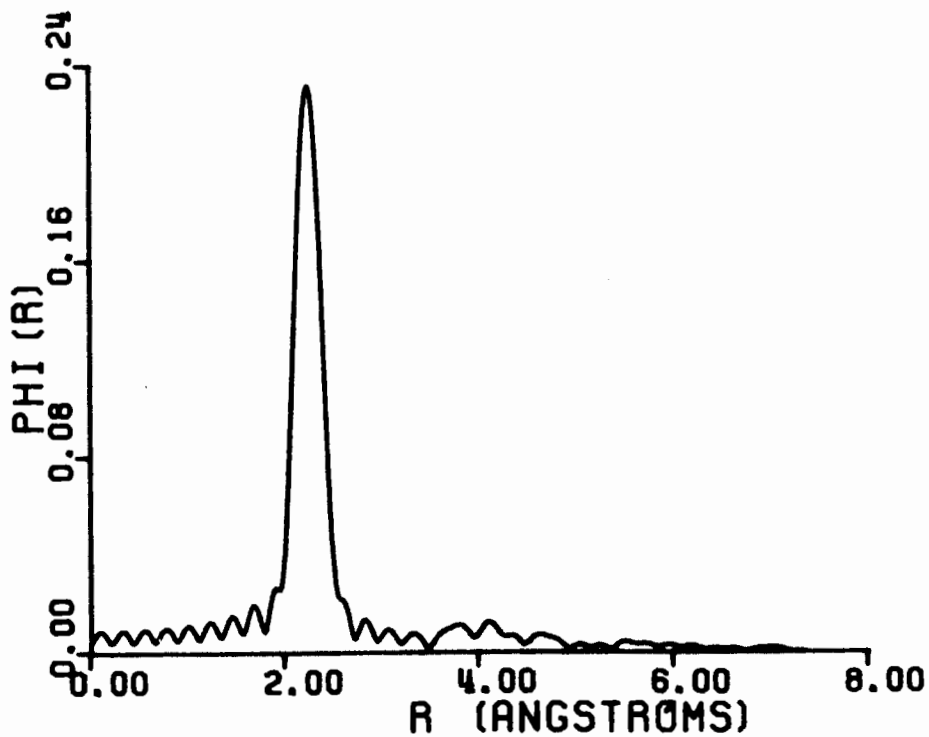

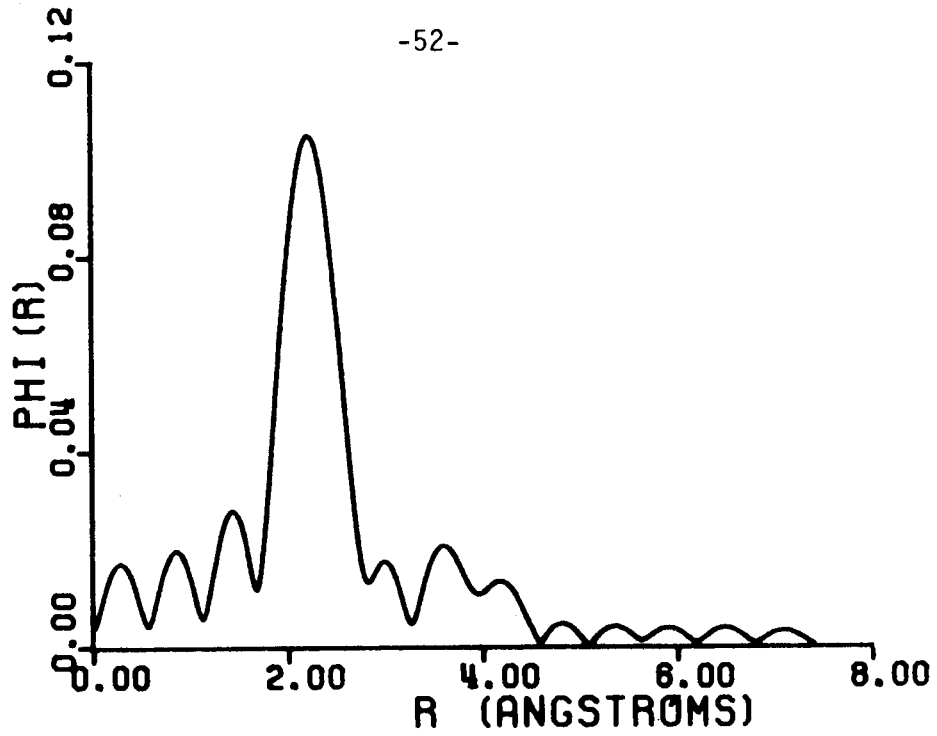Figure 4.8b.   N = 1 transform of CHI from $1.825 - 17.125Å^{\circ-1}$.

Figure 4.9a. N = 1 transform of CHI from 2.425 – 6.675Å^{-1}.
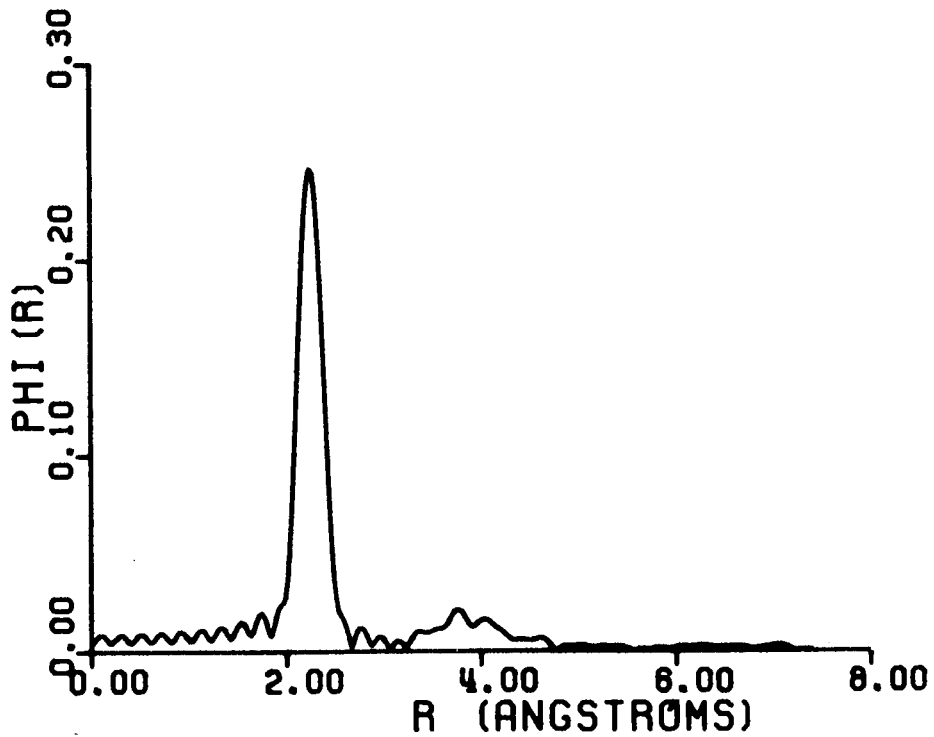

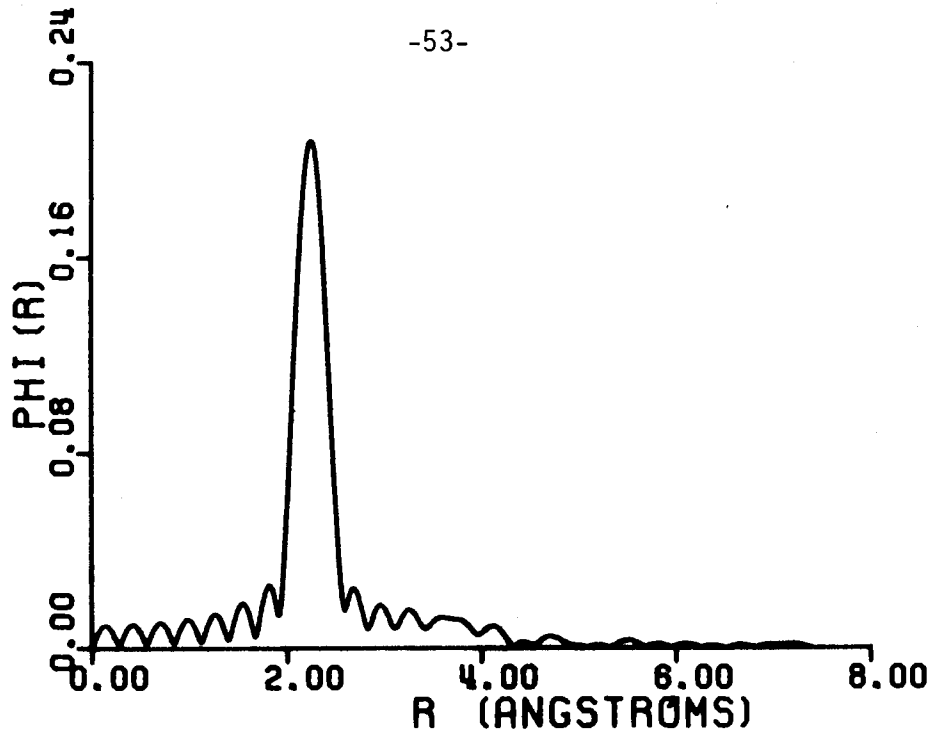Figure 4.9b. N = 1 transform of CHI from 2.425 – 16.425Å^{-1}.

Figure 4.10a. N = 1 transform of CHI from 3.225 - 14.325$\overset{\circ}{A}^{-1}$.
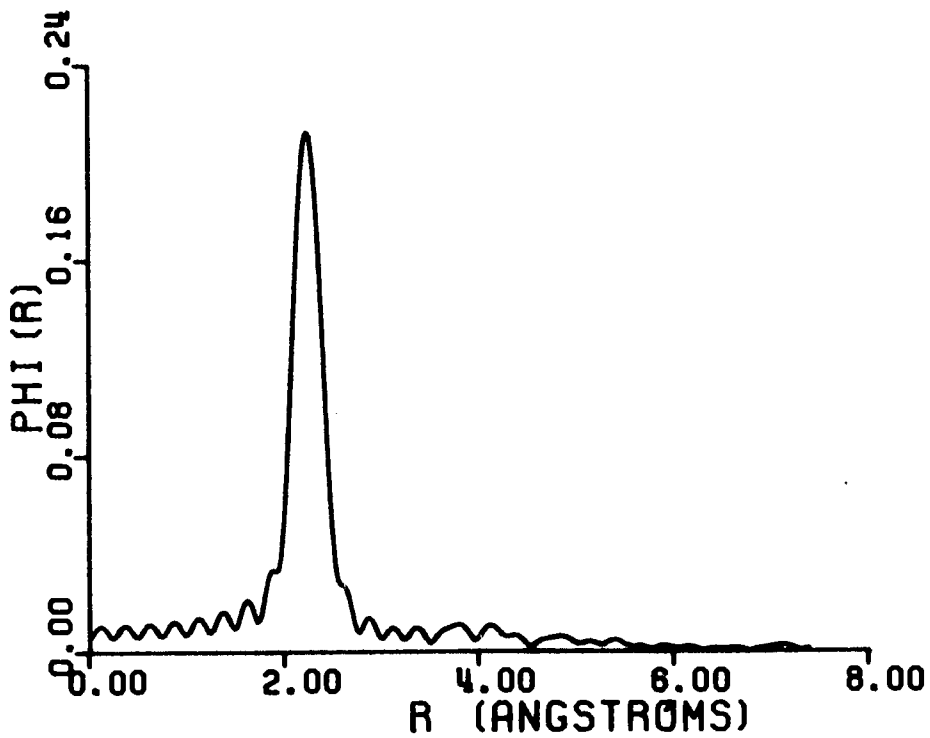

Figure 4.10b. N = 1 transform of CHI from 3.925 - 16.425$\overset{\circ}{A}^{-1}$.

the transform range broadens the nearest neighbor peak. The peak occurs at 2.25Å, as expected, except for the narrowest range transforms. The peaks of Figures 4.8a and 4.9a occur at 2.23Å and 2.21Å respectively. This is an artifact of the narrowness of the window function. The most important point, however, is that when k_{min} is as large as 3 or 4 $Å^{-1}$ structure beyond the nearest neighbor distribution becomes difficult to distinguish from the artifacts of the transform. All that we have said above about low k information is recalled.

Section 4.4 - Fourier Transform Analysis, Part II

The Fourier transform technique may be used to evaluate the structural disorder of the nearest neighbor distribution. If Eqn. 4.1 is multiplied by k/T(k), the only explicit k-dependence remaining is the oscillatory sine term. However, as previously discussed, the oscillations are damped due to the disorder of the system. If the average density function for the nearest neighbor distribution is gaussian, the oscillations are damped by $e^{-2k^2\sigma_1^2}$. A plot of the logarithm of the envelope of k-CHI/T(k) (LNENV) vs. k^2 will then have slope $-2\sigma_1^2$.

This analysis was first applied to the nearest-neighbor-only contribution to CHI. LNENV vs. k^2 is shown in Figure 4.11a. The linearity of this plot indicates the appropriateness of the gaussian assumption. We obtained $\sigma_1^2 = .00091Å^2$, in excellent agreement with Table 4.1

To apply this technique to analyzing a Fourier transform, such as that of Figure 4.6a, requires isolating the first peak. A glance at Figure 4.5 and 4.6a shows that, because of transform artifacts, there is
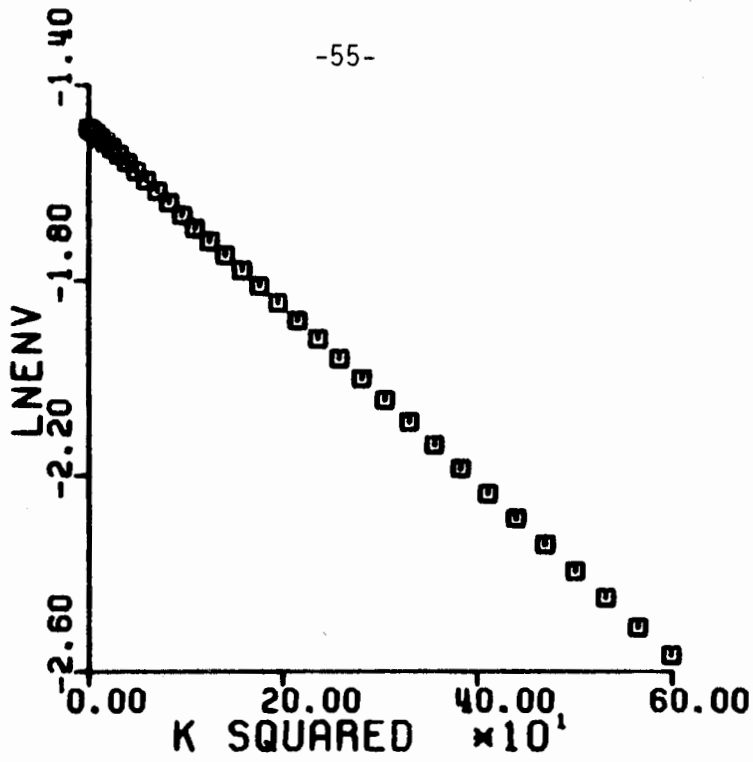
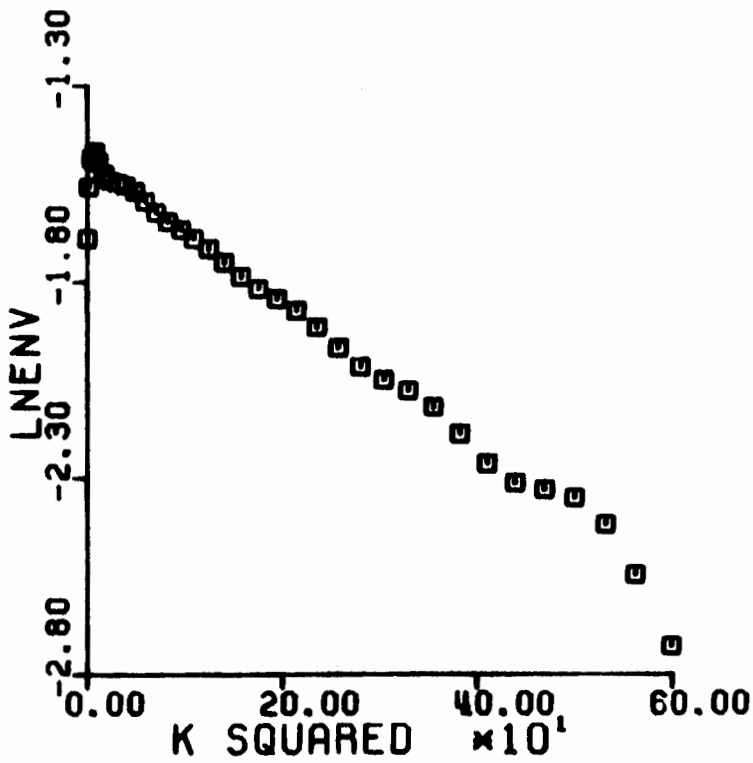Figure 4.11a. LNENV vs. k^2 for the nearest-neighbor only contribution to CHI.

Figure 4.11b. LNENV vs. k^2 for the first peak isolated from the full CHI.

no place where the first peak ends and the second one begins (unlike Figure 4.1b). This means that a small amount of first peak information is lost, and a small amount of leakage from the second and higher peaks is present in any effort to isolate the first peak.

It was found that the best results were obtained by considering the first peak as extending from $r = 0$ to the minimum (the lowest) just beyond $3\overset{\circ}{A}$ (Figure 4.6a). The reverse transform of this peak was taken to isolate the first neighbor contribution to CHI. LNENV vs. k^2 for this function is shown in Figure 4.11b. It is approximately linear. Since there is second neighbor contamination deviation from linearity is expected, especially for low k. Loss of some first neighbor information is also expected to contribute to this. A linear fit was done excluding the first three points. We obtained $\sigma_1^2 = .00094\overset{\circ}{A}^2$, in excellent agreement with the above calculation and Table 4.1.

It is thus possible to obtain accurate information on the structural disorder of the nearest neighbor distribution via the Fourier analysis of the EXAFS. Since the disorder due to thermal vibrations can be calculated for a model structure (J.C. Rehr, to be published), nearest neighbor disorder provides a basis for comparison of model with experiment.

Since models are more distinguishable at larger r, it is of interest to look at what remains after isolation of the first peak. The Fourier transform of what remains is shown in Figure 4.12a. For comparison, the transform of CHI minus the calculated first neighbor contribution is shown in Figure 4.12b. Clearly not too much information has been lost by the process of isolating the first peak.
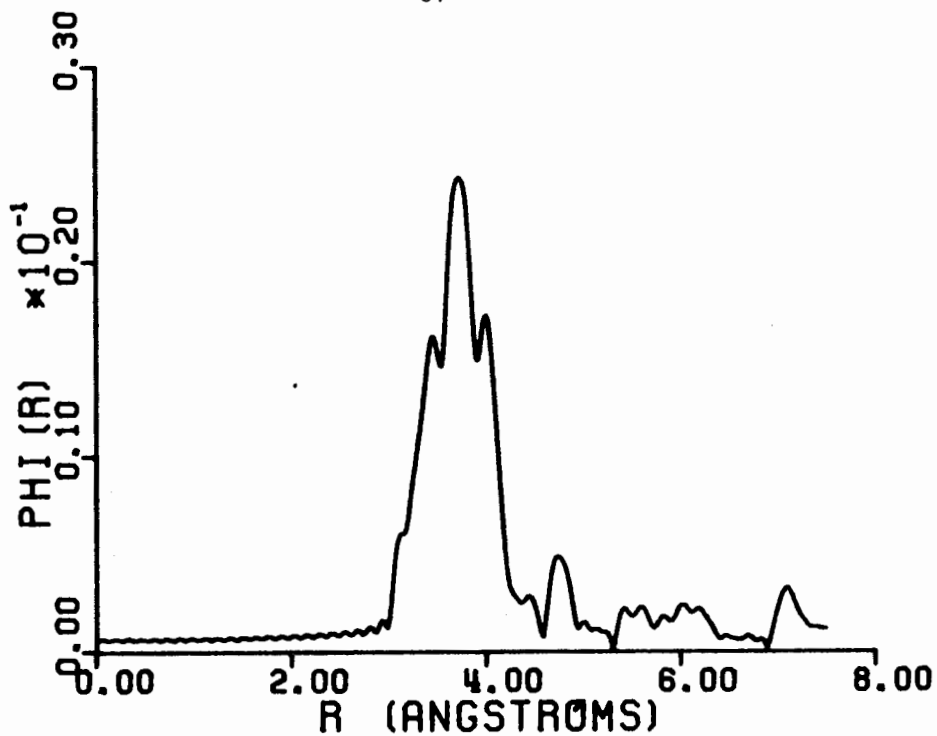
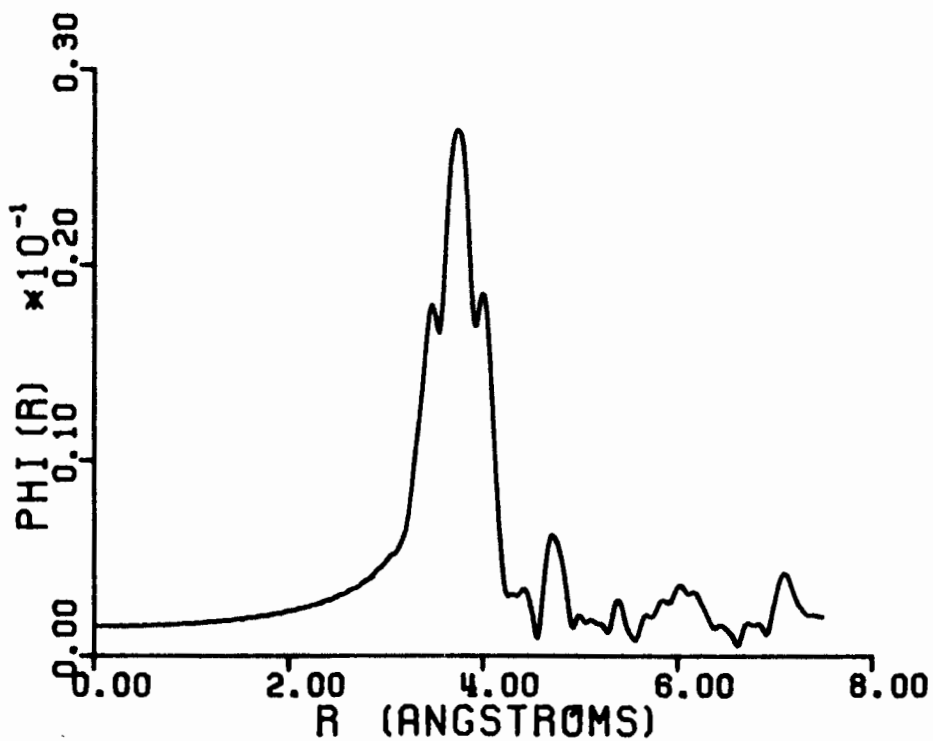Figure 4.12a. N = 1 transform of CHI minus the isolated first peak. (Range: .325 - 24.275Å⁻¹.)

Figure 4.12b. N = 1 transform of CHI minus the nearest neighbor contribution. (Range: .225 - 24.425Å⁻¹.)

These figures are nice from an academic point of view, but unrealistic from the experimental side. For comparison of models, transforms like Figure 4.6a would be excellent. However, as we have seen several times now, revelation of this much structure results from low k information. For sufficiently low energies EXAFS data is not interpretable.

Section 4.5 - Comparison With Experiment

The EXAFS of amorphous germanium, extracted from experimental data taken at 20°C (E.D. Crozier, unpublished), is shown in Figure 4.13a. A comparable portion of the model EXAFS is shown in Figure 4.13b. Comparing the experimental data with the model spectrum, we make four observations. First, the smoothness of the experimental data is interupted by some jaggedness at higher k. This is attributed to background noise in the experimental arrangement (E.D. Crozier, private communication). Second, below $4\overset{\circ}{A}^{-1}$ the oscillations are much reduced in amplitude. This is the region where the assumptions of the EXAFS formalism break down, and comparisons cannot be made in this part of the spectrum. Third, the experimental data also shows reduced oscillations at higher k. This is expected. The data was taken at 20°C so that there is additional disorder in the system which leads to additional damping of the oscillations, as we have discussed previously. Fourth, the periods of the oscillations of the two spectra are slightly different.

Fourier transforms (n = 1) of the two spectra are shown in Figure 4.14. The transform ranges were matched as closely as possible, consistent with the criteria established in Section 4.3. The difference in the oscillation periods of the two spectra results in different peak positions for the nearest neighbor distributions: $2.13\overset{\circ}{A}$ for experiment vs. $2.25\overset{\circ}{A}$ for the model.
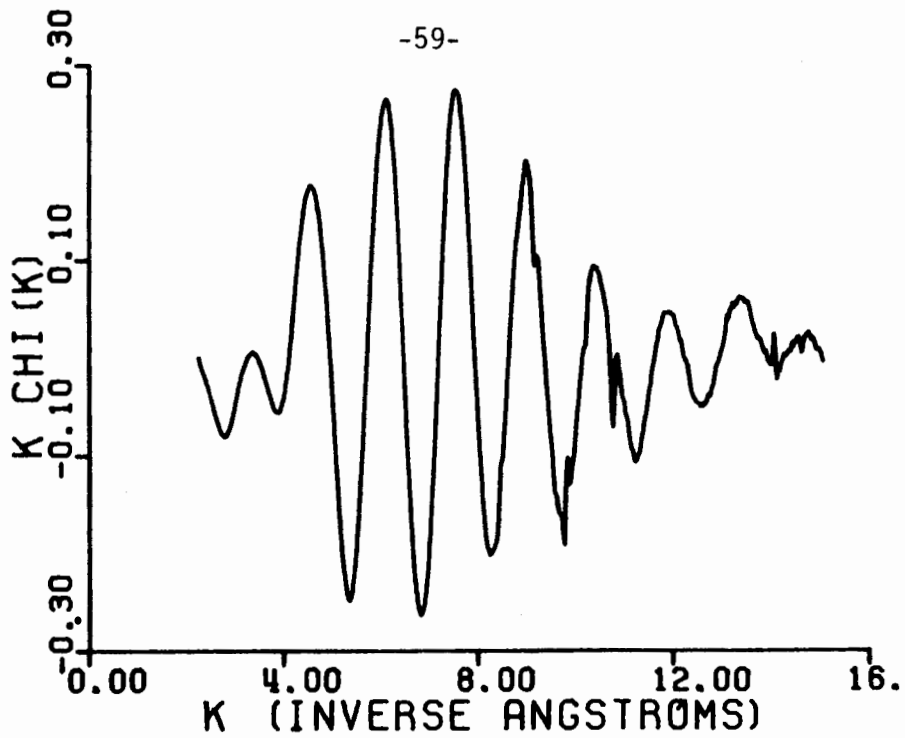
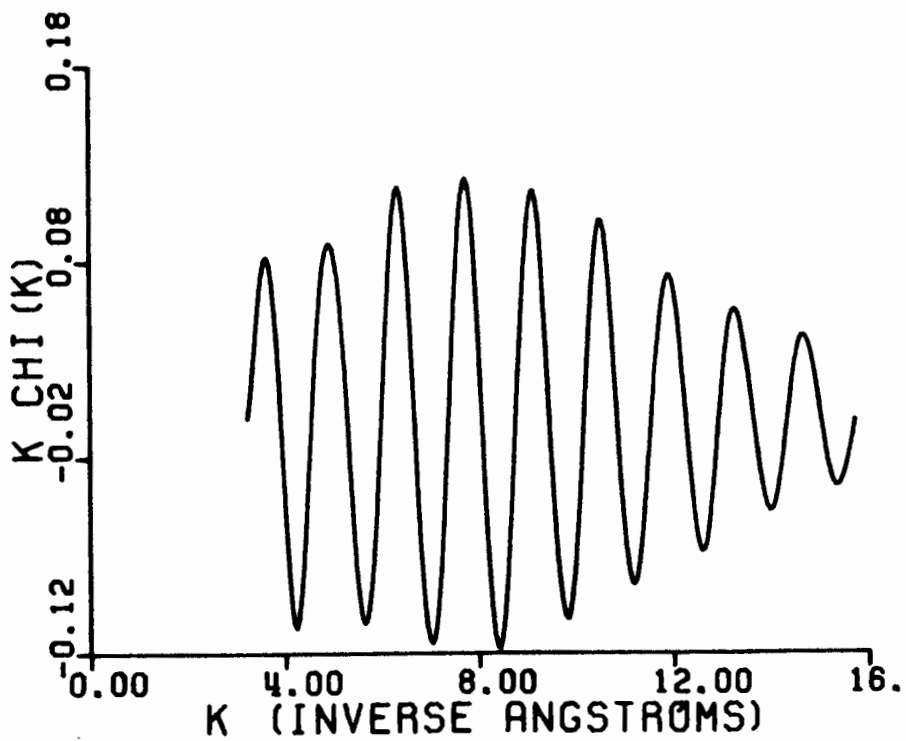Figure 4.13a. Experimental EXAFS of amorphous germanium taken at 20°C.

Figure 4.13b. Model EXAFS for GE.
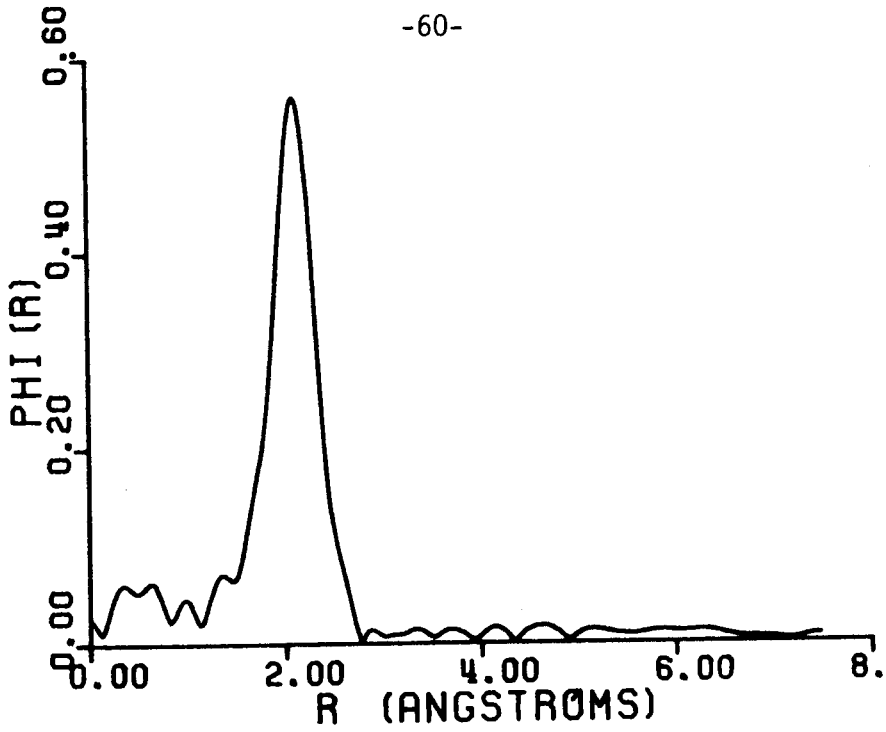
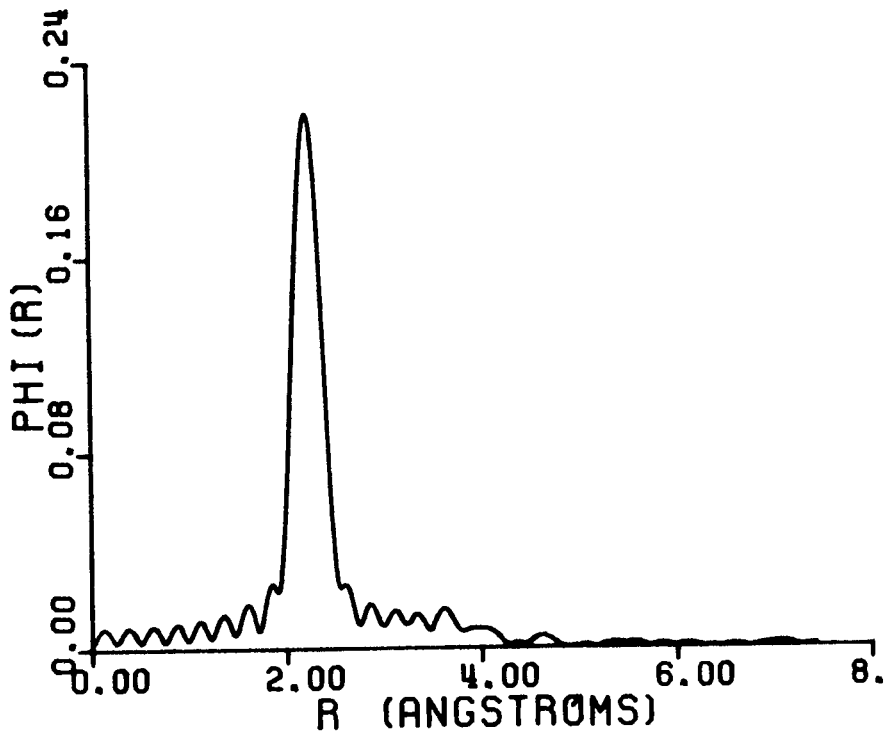Figure 4.14a. N = 1 transform of experimental data on a-Ge from 3.472 – 15.084Å^{-1}.

Figure 4.14b. N = 1 transform of model EXAFS from 3.225 – 15.725Å^{-1}.

This suggests that the simple form used for the phase shift in the model calculation (Eqn. 4.3) is inappropriate.

We also notice that the experimental peak is broader than the model peak. This is expected because of the increased disorder due to thermal vibrations. (To make a proper comparison it is necessary to have the calculated σ^2 due to the thermal motion of the atoms.) The only other significant structural difference we see is the lump at low r in the experimental data. This is due to incomplete background removal.

This comparison of experiment with the model calculation is inconclusive. We are again faced with the now infamous "low k problem". The structure functions of Figure 4.14 reveal nothing beyond the nearest neighbor distributions. The best we can say is that our model remains a possible candidate.

Section 4.6 - Summary and Conclusions

There are two themes upon which this chapter has been developed, both centering on the usefulness of the EXAFS as a tool for structural investigation. What are the limitations of this technique? How useful is it in distinguishing between competing structural models?

We have calculated the EXAFS for the CRN model for amorphous germanium. The Fourier transform was used to generate a radial structure function which compared favourably with the histogram of the ARDF of the model. The structural contribution to the disorder of the nearest neighbor distribution was accurately extracted. But the success of these endeavors depended upon analyzing the EXAFS spectrum below 4Å^{-1}. When we excluded this region, in which the theory is not valid, we found that nothing beyond

the nearest neighbor distribution could be determined. This is due to the damping of the higher neighbor oscillations which arises from the increased disorder encountered in an amorphous material. When we made a realistic comparison with some experimental data we found that nothing beyond the nearest neighbor distribution could be determined.

We draw two conclusions. First, there is an inherent limitation of the EXAFS technique due to the inability to interpret the spectrum for sufficiently low energies. This is critical in a disordered system becuase of the damping of the oscillations due to the disorder. For an amorphous material one is limited to information concerning the nearest neighbor distribution only.

(This conclusion may be overly pessimistic. Some recent work by Crozier (private communication) suggests that it may be possible to extract information about the second neighbor distribution through a technique which involves the use of the Fourier Transform in conjunction with curve-fitting procedures.)

Second, because of the "low k problem", the EXAFS technique, as it has been applied in this work, is of limited usefulness in distinguishing between competing structural models. Success in doing this is contingent upon developing better methods for analyzing EXAFS data.

Chapter 5 - Analysis of a DRPHS Model

In this chapter we apply the EXAFS formalism to a dense-random-packing-of-hard-spheres model. In particular we choose the amorphous binary system of Nickel and Phosphorus.

In Section 5.1 we discuss the model. In Section 5.2 the EXAFS is calculated and analyzed via the Fourier Transform. Multiple scattering is treated in Section 5.3. In Section 5.4 we consider the effects of asymmetric distributions. A summary and some conclusions are presented in Section 5.5.

Section 5.1 - Analysis of the Model

The diameters of Ni and P are within 3% of each other. As shown by Cargill (1970) the Ni-P system can be modeled with single-size spheres of radius $r = 1.21\overset{o}{A}$ (see Figure 3.3).

A 4000-atom cluster of single-size spheres was generated by a program like that described in Section 3.3. A random number generator was then used to label the atoms type 1 (Ni) or 2 (P). The resulting composition is 79% Ni, 21% P, within the composition range that can be prepared in the amorphous state.

Histograms were constructed using central groups of 200, 400, ..., 1200 atoms. There is very little difference in these. The 400-atom average is shown in Figure 5.1.

This distribution shows less structure than the CRN model. There is a sharp peak centered at 2 radii $(2.42\overset{o}{A})$ corresponding to those atoms essentially in direct contact with the central atom. The only other distinctive feature is the sharp drop in the distribution after the peak at 4 radii $(4.84\overset{o}{A})$ has been reached. The distribution is otherwise bland. Notice that,
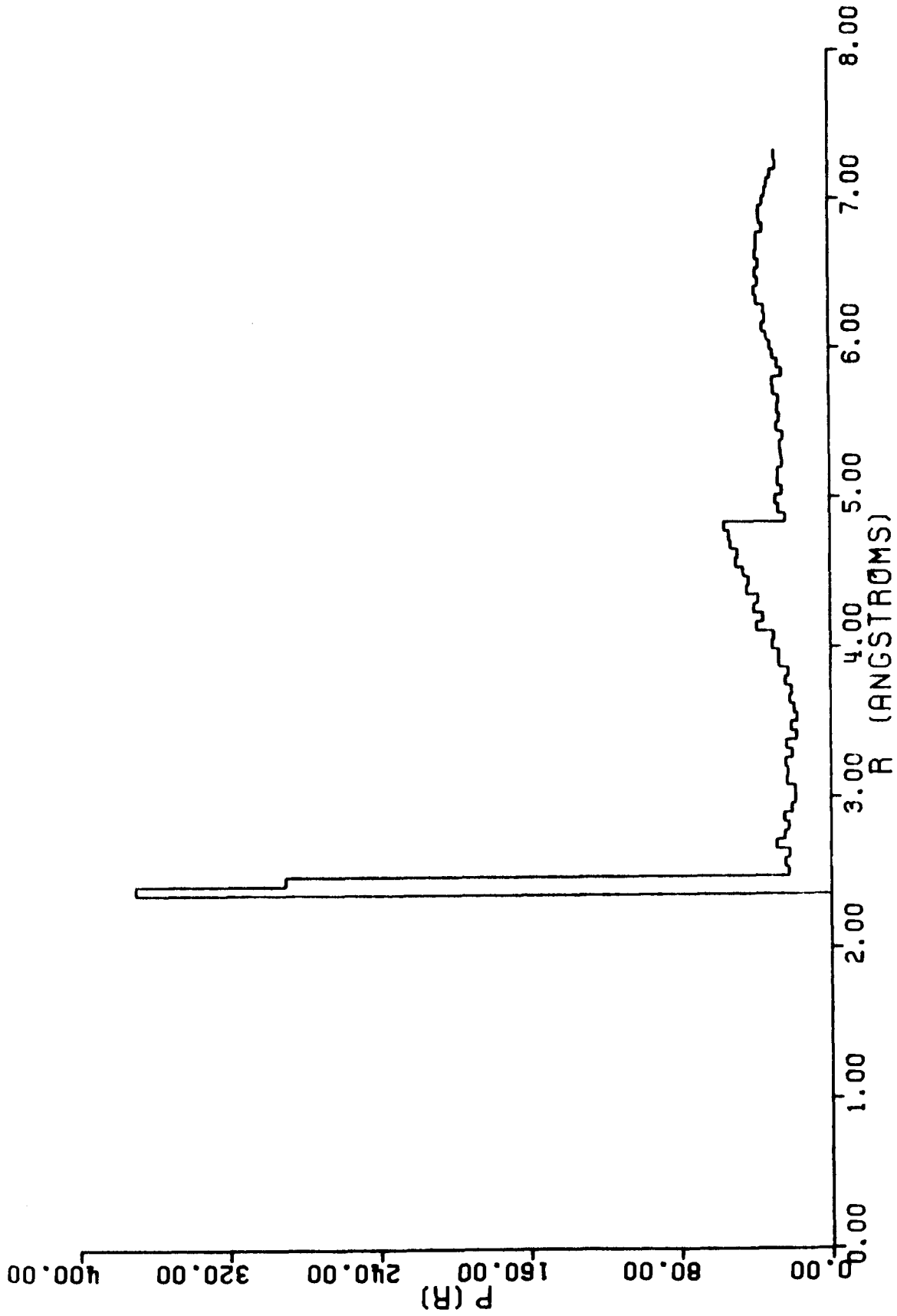
Figure 5.1. Average radial density function for the hard sphere cluster averaged over 400 atoms.

in contrast to the CRN model, the concepts of first and second nearest neighbors are not well defined. Thus there is no unambiguous way to calculate, say, $\bar{R}_1$ or $\sigma_1{}^2$.

Section 5.2 - Analysis of the EXAFS

As before we calculate CHI via

$$\chi(k) = \frac{T(k)}{k} \sum_j \frac{e^{-2R_j/\lambda}}{R_j{}^2} \sin(2kR_j + \delta_j(k)). \tag{5.1}$$

The sum is over all atoms within $7.26\overset{\circ}{A}$ of the central atom.

We again use the Lorentzian parameterization for $T(k)$ (Teo et al., 1977). To correct for a sin of omission in the preceding chapter we discuss this more fully here. Teo et al. calculate $T(k)$ by the formalism of Lee and Beni (1977) who use a complex potential to calculate phase shifts. This results in complex phase shifts. The backscattering amplitude calculated this way includes inelastic losses. Our use of the attenuation factor $e^{-2R/\lambda}$ is thus strictly a multiple scattering correction. (Since there is no multiple scattering correction for the first shell a more appropriate factor is $e^{-2(R-\bar{R}_1)/\lambda}$, where $\bar{R}_1$ is the first peak position. But this amounts to a constant scaling factor which we ignore.) We set $\lambda = 5.0\overset{\circ}{A}$.

Lee et al. (1977) have calculated phase shifts according to the Lee and Beni formalism. They parameterized these over the range $4\text{-}16\overset{\circ}{A}{}^{-1}$ according to

$$\delta(k) = (a_0 + b_0 - \pi) + (a_1 + b_1)k + (a_2 + b_2)k^2 + (a_3 + b_3)/k^3, \tag{5.2}$$

where a and b represent the absorbing and backscattering atoms respectively.

The parameters for T(k) and δ(k) are listed in Table 5.1. Values interpolated from the Lee et al. data are so indicated.

We confine our attention to the central group of 500 atoms, of which 396 are Ni and 104 are P. We calculate the EXAFS averaged over each of these groups. Figure 5.2 shows the EXAFS for the P K-edge, and the $n = 1$ Fourier Transform of this data from 4.125 - 15.1625$\overset{o}{A}^{-1}$. (Applying the same convention as in the preceding chapter, transforms are taken between points where CHI $\approx$ 0 such that an integral number of oscillations of the EXAFS are included.) Figure 5.3 shows the corresponding plots for the Ni K-edge. The transform range is 3.875 - 15.625$\overset{o}{A}^{-1}$.

Unfortunately these figures are not very revealing. The two EXAFS spectra are virtually identical. The transform of the P EXAFS has a peak at r = 2.15$\overset{o}{A}$; that of the Ni EXAFS at 2.11$\overset{o}{A}$. (The actual distribution peaks at 2.42$\overset{o}{A}$.) Some difference is expected since the central atom phase shift is different in both cases. But, looking at Eqn. 5.2, it is not obvious what kind of shift in the peak position we should expect to see. In either case the shift is less than can be accounted for by the linear term alone.

Beyond the first peak any structure present is buried by the transform wiggles. This is expected since we have no low k information (recalling the discussion in Chapter 4). Our analysis ends before it begins. While we have the spectra of two edges to look at, there is no evidence that we can distinguish between the different types of atoms in either. Even though the atoms are the same size, Ni and P have different scattering properties and we might expect to see something. We don't.

Table 5.1

Parameters for Ni and P

a. Backscattering Amplitude (Magnitude).

	$A(\overset{\circ}{A})$	$B(\overset{\circ}{A})$	$C(\overset{\circ}{A}^{-1})$	
Ni	.65	.187	7.04	(interpolated)
P	.747	.2402	3.258	

b. Phase shift due to backscattering atom.

	b_0	$b_1(\overset{\circ}{A})$	$b_2(\overset{\circ}{A}^2)$	$b_3(\overset{\circ}{A}^{-3})$	
Ni	7.0	-.205	0	-97	(interpolated)
P	4.919	-.3743	.00619	0	

c. Phase shift due to absorbing atom.

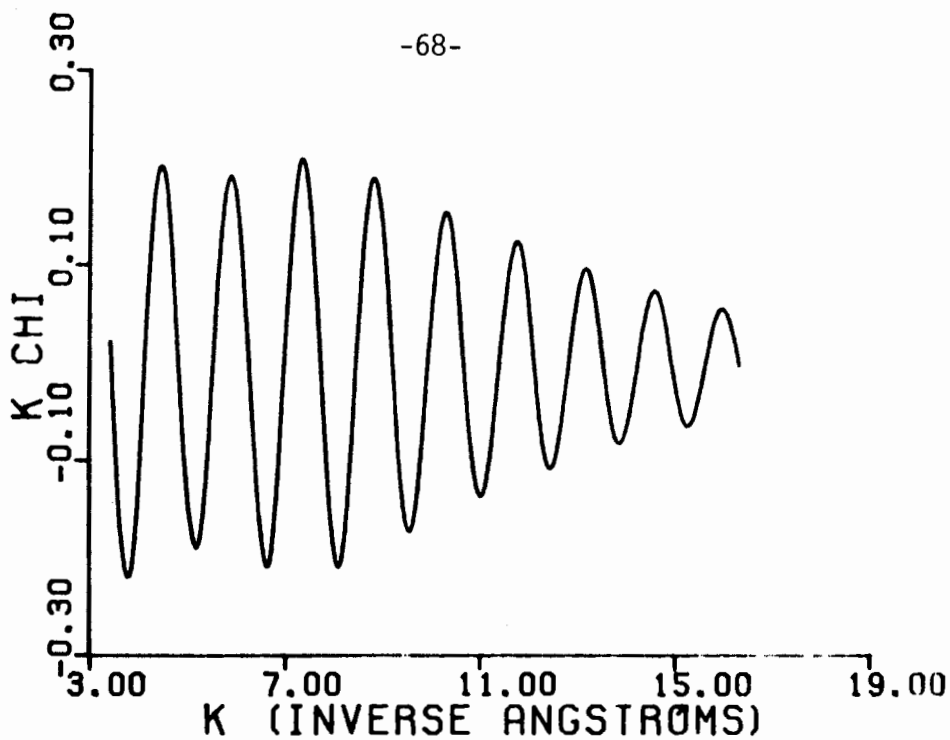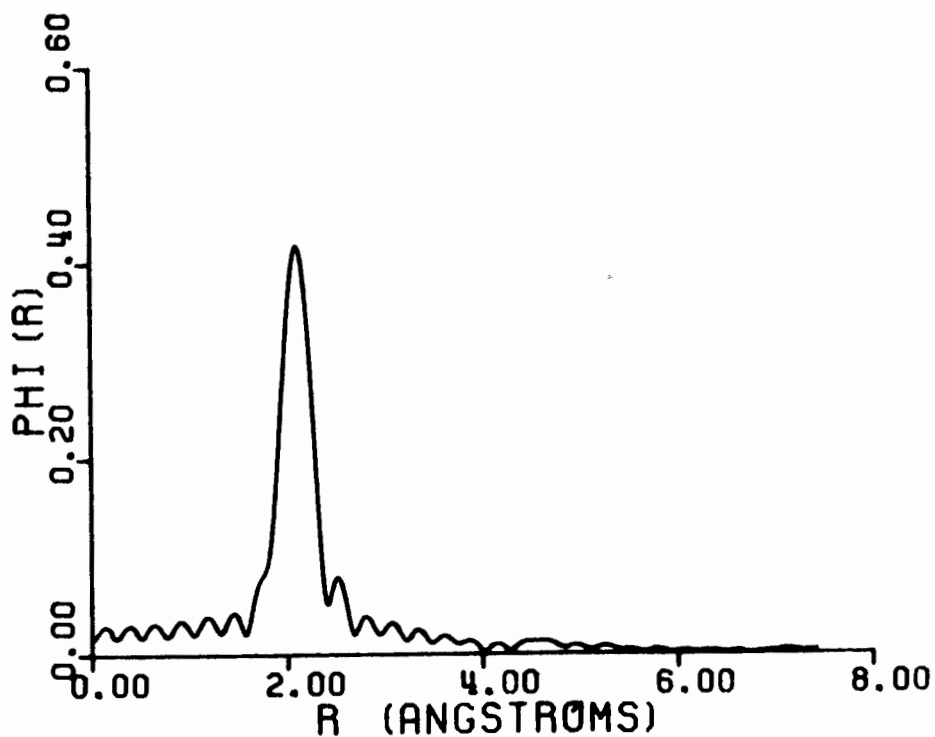|	a_0	$a_1(\overset{\circ}{A})$	$a_2(\overset{\circ}{A}^2)$	$a_3(\overset{\circ}{A}^{-3})$	
Ni	5.0	-.96	-.0247	25.5	(interpolated)
P	.20	-.84	-.0237	25.0	(interpolated)

Figure 5.2a. K-CHI for the P edge of NiP.

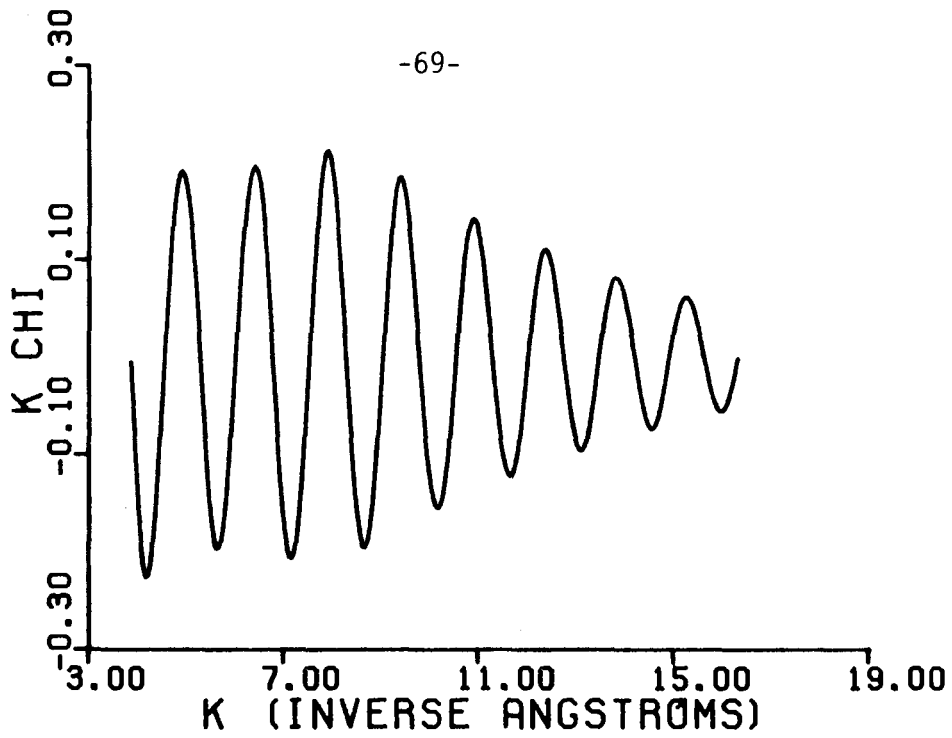Figure 5.2b. N = 1 transform of the above EXAFS from
4.125 - 15.625Å^{-1}.

Figure 5.3a. K-CHI for the Ni edge of NiP.
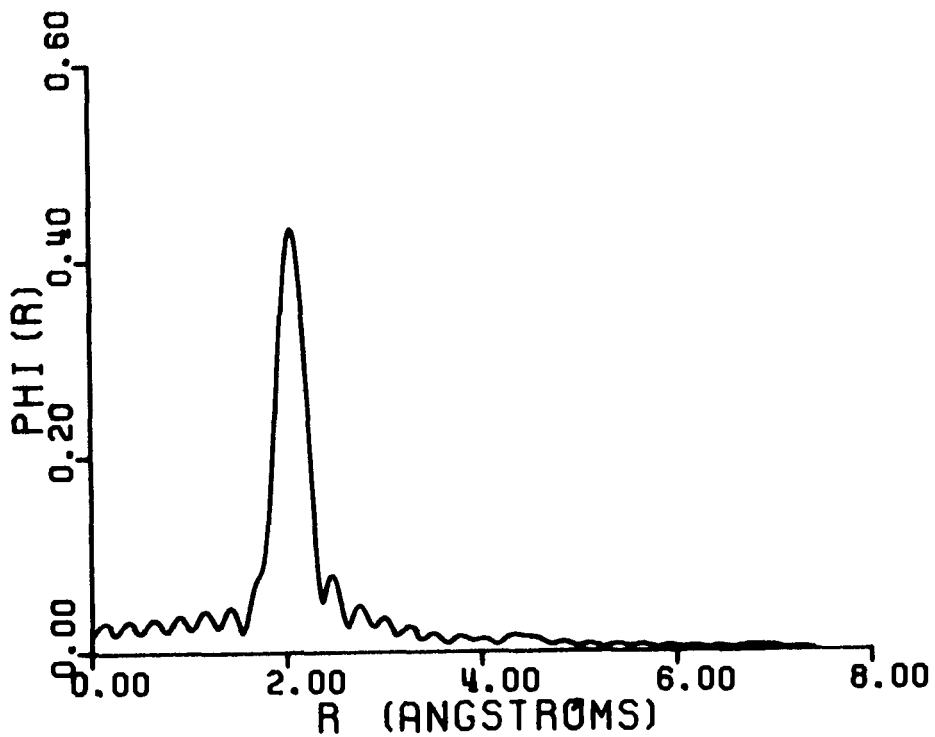

Figure 5.3b. N = 1 transform of the above EXAFS from
3.875 - 15.625Å^{-1}.

Section 5.3 - Multiple Scattering

Since the hard sphere cluster is closely packed we might expect to see a significant multiple scattering contribution to the EXAFS. To calculate this requires solving for the full Green's function (Eqn. 2.37) and using Eqn. 2.43. But this requires matrix inversion techniques (and computer time) beyond the scope of this thesis.

We can hope to get some physical insight into this problem by considering the case of s-wave-only ($\ell = 0$) scattering. (This is the approach Ashley and Doniach (1975) take for the crystalline case.) In this case Eqns. 2.37 and 2.43 reduce to

$$G_{\alpha\beta} = G^0_{\alpha\beta} + \sum_{\nu} G_{\alpha\nu} t_{\nu} G^0_{\nu\beta} \quad , \tag{5.3}$$

$$\chi(k) = -\frac{1}{k} \text{Im} \left\{ e^{2i\eta_1} \sum_{\beta \neq \alpha} G_{\alpha\beta} t_{\beta} G^0_{\beta\alpha} \right\} \quad , \tag{5.4}$$

where we have dropped the angular momentum indices to simplify the notation.

As we have seen before only the closest atoms contribute to the EXAFS. We therefore evaluate Eqn. 5.4 for the EXAFS due to those atoms within 4.84Å of the absorbing atom. This particular choice of cutoff is suggested by the sharp drop in the distribution at this point (see Figure 5.1). Within this range are approximately 50 atoms.

While the solution of Eqn. 5.3 is easy to set up, it requires a great deal of computer time. Since we require an averaging over some significant number of atoms we had to abandon this approach. Instead we chose to calculate only the single and double scattering contributions (χ_S and χ_D) by iterating Eqn. 5.4 by Eqn. 5.3. To further simplify we set $t(k) \sim 1/k$

for both atomic species. This leads to the simple analytic expression

$$\chi_S(k) + \chi_D(k) = -1/k^2 \sum_{\beta \neq \alpha} \frac{1}{R_{\alpha\beta}^2} \sin (2kR_{\alpha\beta} + 2\eta_1)$$

$$-1/k^3 \sum_{\beta,\nu} \frac{1}{R_{\alpha\beta}R_{\beta\nu}R_{\nu\alpha}} \sin [k(R_{\alpha\beta} + R_{\beta\nu} + R_{\nu\alpha}) + 2\eta_1].$$

$$(5.5)$$

This was calculated, averaging over the 104 P atoms mentioned above. An attenuation factor with $\lambda = 10\overset{\circ}{A}$ was included.

Figure 5.4a shows the single scattering contribution, while Figure 5.4b shows the single plus double scattering contribution to the EXAFS. Any difference is not clearly visible. In fact there is only the slightest difference below $7\overset{\circ}{A}^{-1}$. The corresponding n = 1 transforms are shown in Figure 5.5. Here again the differences are small. The first peaks are identical (at r = $2.23\overset{\circ}{A}$) while some slight differences occur at large r. It appears that, at least for the energy range above $4\overset{\circ}{A}^{-1}$, multiple scattering is not important in this system.

Section 5.4 - Asymmetry

It is clear from Figure 5.1 that the first neighbor distribution, no matter how it is defined, is asymmetric. Eisenberger and Brown (1978) have shown how to expand CHI about the mean first neighbor separation $\bar{r}$:
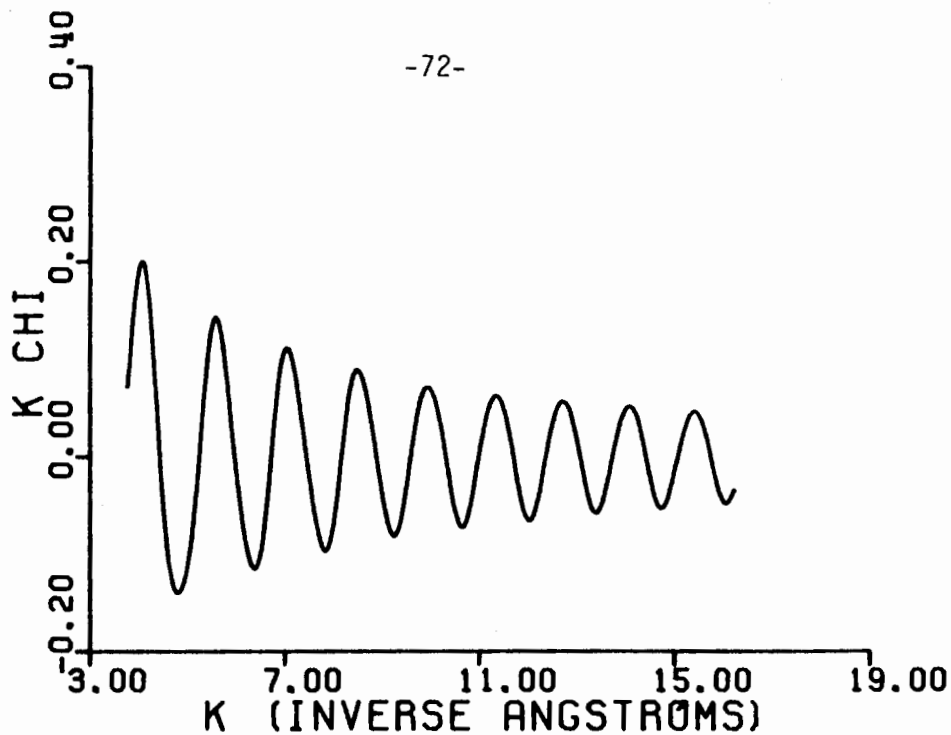
Figure 5.4a. Single scattering EXAFS.
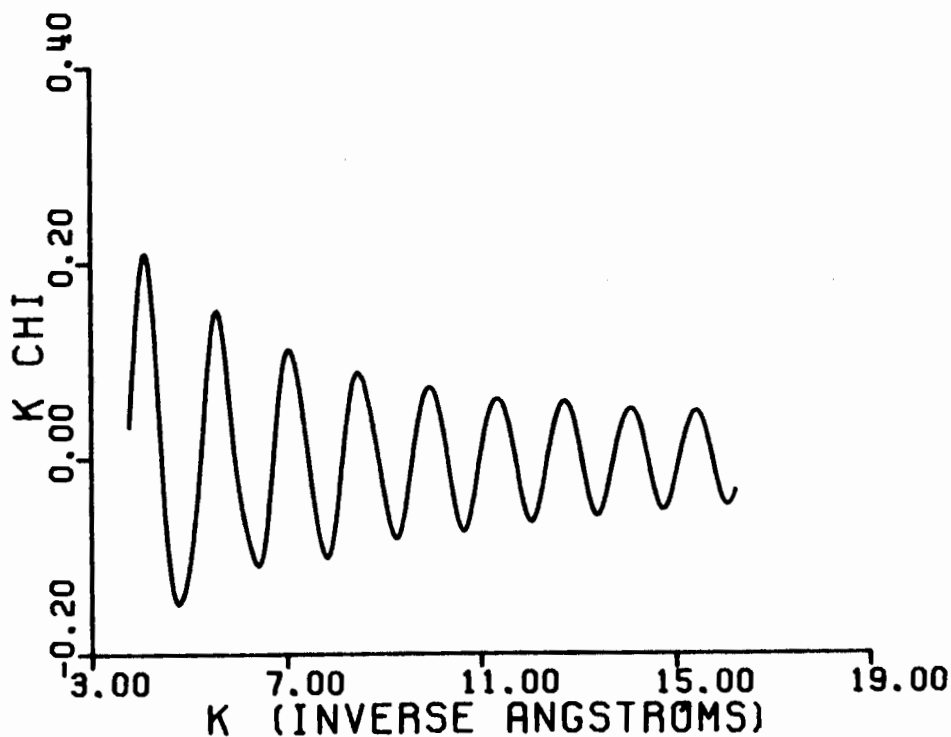

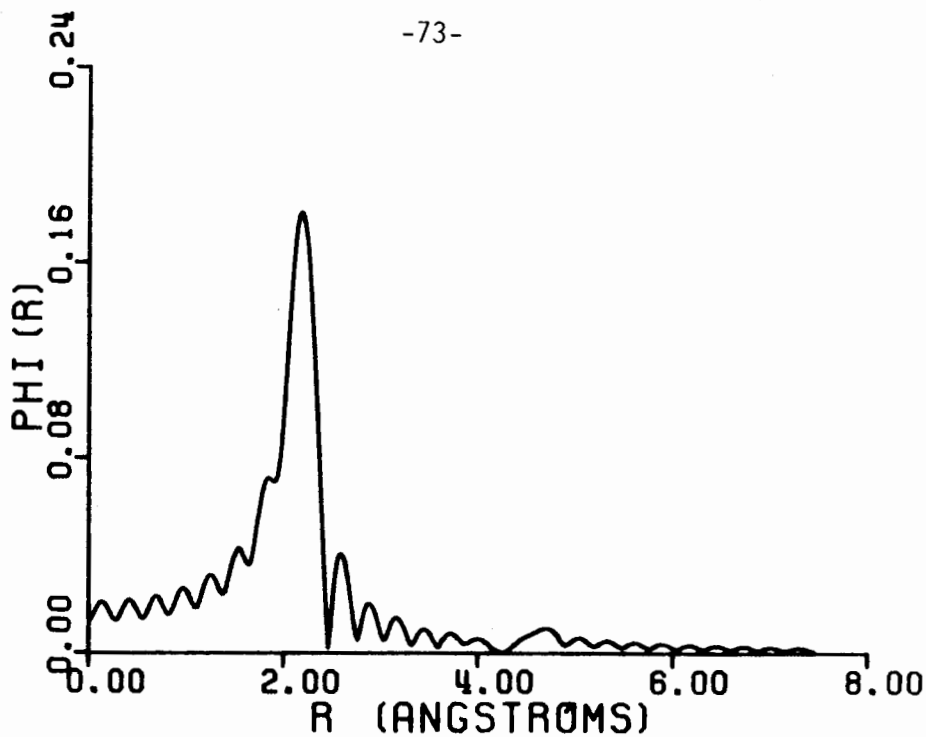Figure 5.4b. Single plus double scattering EXAFS.

Figure 5.5a. N = 1 transform of single scattering EXAFS from 4.425 - 15.775Å⁻¹.
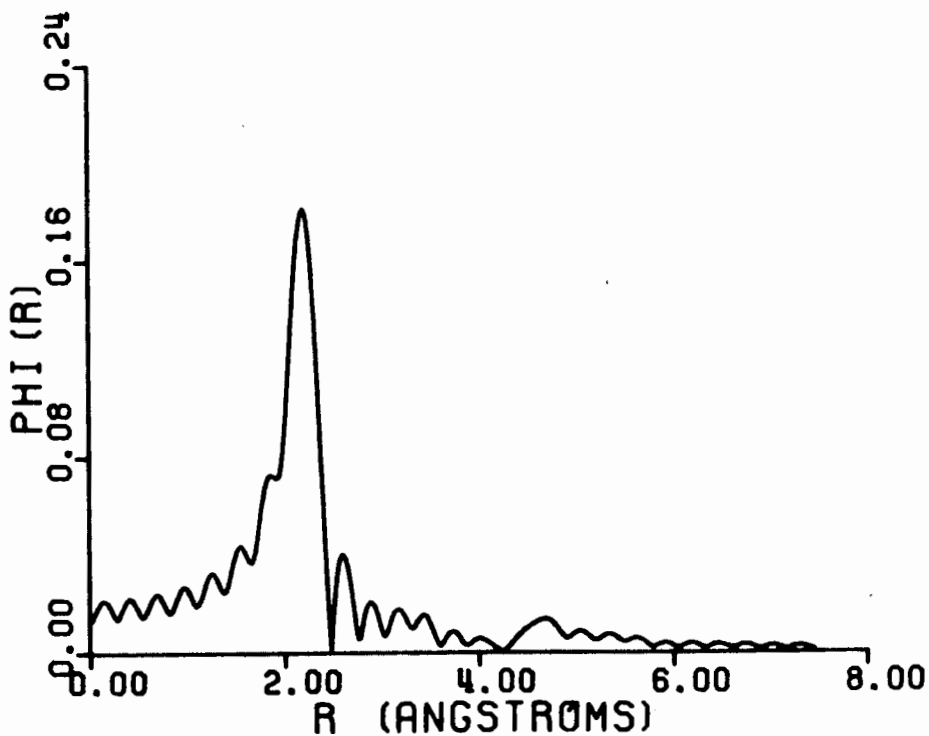
Figure 5.5b. N = 1 transform of single plus double scattering EXAFS from 4.425 - 15.775 Å⁻¹.

$$\chi(k) \;=\; \frac{T(k)}{k} \left[S^2(k) + A^2(k) \right]^{\frac{1}{2}} \; \sin(2k\bar{r} + \delta(k) + \textstyle\sum(k)), \tag{5.6}$$

where

$$\textstyle\sum(k) \;=\; \tan^{-1} \frac{A(k)}{S(k)} \;, \tag{5.7}$$

and

$$A(k) \;=\; \int_{-\infty}^{\infty} g(\bar{r} + x) \sin 2kx \; dx \;, \tag{5.8}$$

$$S(k) \;=\; \int_{-\infty}^{\infty} g(\bar{r} + x) \cos 2kx \; dx \;. \tag{5.9}$$

Here $x = r - \bar{r}$, g is the first neighbor distribution function, and $T(k)$ and $\delta(k)$ are defined as before. An attenuation factor may be included in g.

In general, of course, the distribution function is not known. In our case we know the exact distribution, but we can consider this in a more ideal way by looking at some simple analytic expressions for g. We can calculate CHI by

$$\chi(k) \;=\; \int_{0}^{\infty} g(r) \sin 2kr \; dr \;, \tag{5.10}$$

neglecting the scattering parameters.

We consider two cases:

(1) $g(r)$ = $\begin{cases} 10, & 1.9 \leq r \leq 2.1 \\ 1, & 2.1 < r \leq C \\ 0, & \text{elsewhere} \end{cases}$ (5.11)

where we let C vary from 2.1 to 4.1;

(2) $g(r)$ = $\begin{cases} (r - r_0)e^{-(r - r_0)}, & r \geq r_0 \\ 0, & r \leq r_0 \ . \end{cases}$ (5.12)

To examine the effects of asymmetry we calculate CHI by Eqn. 5.10, Fourier Transform CHI and locate the peak. Then we calculate $\sum(k)$ by Eqns. 5.7 - 5.9 and examine this in terms of Eqn. 5.6.

For case 1 both the magnitude and imaginary part of the Fourier Transform peak at $r = 2.0$ for any value of C considered. There is no shift in the peak position. For $C = 4.1$, $\sum(k)$ is practically linear in k with a coefficient of $-1.10\overset{\circ}{A}$. From Eqn. 5.6 we expect to see a peak at $\bar{r} - .55\overset{\circ}{A}$, and this is what we see ($\bar{r} = 2.55\overset{\circ}{A}$).

The asymmetry of case 2 is more extreme. Using Eqn. 5.10 we get

$$\chi(k) = \frac{(1 - 4k^2) \sin 2kr_0 + 4k \cos 2kr_0}{(1 + 4k^2)^2}$$

$$= \frac{\sin (2kr_0 + \sum_2(k))}{1 + 4k^2} ,$$ (5.13)

where

$$\Sigma_2(k) = \tan^{-1}\left(\frac{4k}{1-4k^2}\right).$$ (5.14)

The function $g(r)$, given by Eqn. 5.12, peaks at $r_0 + 1$, and $\bar{r} = r_0 + 2$. While the imaginary part of the Fourier Transform peaks at $r_0 + 1$, the magnitude peaks at $r_0 + .31\overset{\circ}{A}$ ($\bar{r} - 2.0 + .31$). $\Sigma(k)$ is practically linear with a coefficient of $-4.0\overset{\circ}{A}$. Thus, from Eqn. 5.6, we expect a peak at $\bar{r} - 2.0$ (r_0). We reach a similar conclusion by looking at Eqns. 5.13 - 5.14. The phase shift $\Sigma_2(k)$ is linear for small k ($\lesssim .5\overset{\circ}{A}^{-1}$) and approaches zero like $-1/k$.

This last case gives us an important result, especially since Eqn. 5.12 is a physically realistic distribution. First, for a sufficiently asymmetric distribution, the magnitude of the Fourier Transform shows a shift in the peak position due solely to asymmetry. Second, the magnitude and imaginary part of the Fourier Transform do not peak in the same place. Recalling the discussion of Section 2.5 we see that, in this case, knowledge of the phase shifts cannot be used to determine $k = 0$. Both of these points indicate that further analysis of the effects of asymmetry on the EXAFS is required in order to properly analyze experimental data.

Section 5.5 - Summary and Conclusions

In this chapter we have calculated the EXAFS for the DRPHS model for amorphous NiP. The Fourier Transform was used to generate a radial structure function. As we have come to expect, the lack of low k information makes it impossible to extract meaningful information about structure beyond the nearest neighbour distribution. We found that, even with two absorption edges

to look at, we could not obtain any information regarding, say, the P-P or P-Ni distributions.

Complications regarding the analysis of the EXAFS involve possible multiple scattering effects and the effects of asymmetric distributions. We calculated the s-wave double scattering contribution and found that it was not important in this system. We also calculated the effects of asymmetry for some model distributions. We found that while the position of the first peak of the Fourier Transform may be shifted, the shift appears to be much smaller than expected (Eisenberger and Brown, 1978).

We conclude that the problems to be encountered in the analysis of the EXAFS are formidable.

Chapter 6 - Summary and Conclusions

We have calculated the EXAFS of two structural models for disordered systems; a CRN model for semiconductors, and a DRPHS model for metallic systems. In both cases the EXAFS was analyzed via the Fourier Transform Technique.

In a disordered system the degree of disorder increases as a function of r. As we have seen, increased disorder leads to increased damping of the oscillations of the EXAFS as a function of energy. We find that information about the distribution beyond the first neighbors is effectively damped out for $k \gtrsim 4 \, \text{Å}^{-1}$. But the existing formalism is a high-energy approximation which is valid only in this range. We conclude that, for the investigation of disordered systems, the EXAFS technique is limited to obtaining information about nearest neighbor distributions. Because of this we further conclude that the analysis of the EXAFS will not be of much use in investigating the appropriateness of particular structural models.

Even in the case of the nearest neighbor distribution there are difficulties with analysis. The position of the peak in the Fourier Transform of the EXAFS depends upon the actual peak position, and the effects of the phase shifts. To extract the actual peak position requires a thorough analysis of the phase shifts involved.

In principle, one can calculate the phase shifts due to the absorbing and back scattering atoms once one has a model for the potentials involved. But we have seen that there may be an additional phase shift due to asymmetry in the real-space distribution. This requires further investigation.

We conclude that while the EXAFS does contain structural information, considerable difficulties remain in analyzing EXAFS data.

APPENDIX A

GAUNT COEFFICIENTS

For a general discussion of the Gaunt coefficients, the reader is referred to Rose (1957, Chapter 3).

The Gaunt coefficients are defined in terms of the integral of three spherical harmonics:

$$C_{L_3 L_2 L_1} = \int d\Omega\, Y_{L_3}^{*}(\theta,\varphi) Y_{L_2}(\theta,\varphi) Y_{L_1}(\theta,\varphi). \tag{A.1}$$

These coefficients vanish unless:

(1) $m_3 = m_2 + m_1$,

(2) $\ell_3 + \ell_2 + \ell_1$ is an even integer ,

(3) $|\ell_3 - \ell_1| \leq \ell_2 \leq |\ell_3 + \ell_1|$. $\tag{A.2}$

Obviously, if one of the Ls is zero, orthonormality of the spherical harmonics leads to

$$C_{L_3 L_2 0} = \frac{1}{\sqrt{4\pi}}\, \delta_{\ell_3,\ell_2}\, \delta_{m_3,m_2}$$

$$C_{0 L_2 L_1} = \frac{1}{\sqrt{4\pi}}\, (-1)^{m_1}\, \delta_{\ell_1,\ell_2}\, \delta_{m_1,m_2} \quad . \tag{A.3}$$

List of References

1. Alben, R., Weaire, D., Smith, J.E. Jr. and Brodsky, M.H., Phys. Rev. B11, 2271 (1975).

2. Ashley, C.A. and Doniach, S., Phys. Rev. B11, 1279 (1975).

3. Azároff, L.V., Rev. Mod. Phys. 35, 1012 (1963).

4. Bell, R.J. and Dean, P., Nature 212, 1354 (1966).

5. Bennett, C.H., J. Appl. Phys. 43, 2727 (1972).

6. Bernal, J.D., Nature 183, 141 (1959).

7. Bethe, H.A. and Salpeter, E.E., "Quantum Mechanics of One and Two-Electron Atoms", Springer-Verlag, Berlin (1957), Sections 59 and 69.

8. Cargill, G.S. III, J. Appl. Phys. 41, 2248 (1970).

9. Cochrane, R.W., Harris, R. and Plischke, M., J. Non-Cryst. Solids 15, 239 (1974).

10. Cohen, M.H. and Turnbull, D., Nature 203, 964 (1964).

11. Eisenberger, P. and Brown, G.S., 1978, to be published.

12. Finney, J.L., Proc. Roy. Soc. (London) A319 , 479 (1970).

13. Keating, P.N., Phys. Rev. 145, 637 (1966).

14. Kostarev, A.I., Zh. Eksperim. i Teor. Fiz. 19, 413 (1949).

15. Kronig, R. de L., Z. Physik 70, 317 (1931).

16. _____ , Z. Physik 75, 191 (1932a).

17. _____ , Z. Physik 75, 468 (1932b).

18. Lee, P.A. and Beni, G., Phys. Rev. B15, 2862 (1977).

19. Lee, P.A. and Pendry, J.B., Phys. Rev. B11, 2795 (1975).

20. Lee, P.A., Teo, B. and Simons, A.L., J. Am. Chem. Soc. 99, 3856 (1977).

21. Lloyd, P. and Smith, P.V., Adv. in Phys. 21, 69 (1972).

22. Messiah, A., "Quantum Mechanics" (2 Vols.), J. Wiley and Sons, New York (1962), Chapters X and XIX.

23. Moss, S.C. and Graczyk, J.F., Phys. Rev. Lett. $\underline{23}$, 1167 (1969).

24. Paul, W., in Proc. of the Intern. Summer School on Physics of Structurally Disordered Solids, Univ. of Rhode Island (1976).

25. Petersen, H., Z. Physik $\underline{80}$, 258 (1933).

26. Polk, D.E., J. Non-Cryst. Solids $\underline{5}$, 365 (1971).

27. Polk, D.E., J. Non-Cryst. Solids $\underline{11}$, 381 (1973).

28. Polk, D.E. and Boudreaux, D.S., Phys. Rev. Lett. $\underline{31}$, 92 (1973).

29. Roman, P., "Advanced Quantum Theory", Addison-Wesley, Reading, Mass. (1965), Chapters 3 and 4.

30. Rose, M.E., "Elementary Theory of Angular Momentum", J. Wiley and Sons, New York (1957), Chapter 3.

31. Sayers, D.E., Lytle, F.W. and Stern, E.A., "Advances in X-Ray Analysis", Vol. $\underline{13}$, 248 (Plenum Press, 1970).

32. Sayers, D.E., Stern, E.A. and Lytle, F.W., Phys. Rev. Lett. $\underline{27}$, 1204 (1971).

33. Shevchik, N.J. and Paul, W., J. Non-Cryst. Solids $\underline{8-10}$, 381 (1972).

34. Shiraiwa, T., Ishimura, T. and Sawada, M., J. Phys. Soc. Japan $\underline{13}$, 847 (1958).

35. Steinhardt, P., Alben, R., Duffy, M.G. and Polk, D.E., Phys. Rev. B$\underline{8}$, 6021 (1973).

36. Stern, E.A., Phys. Rev. B$\underline{10}$, 3027 (1974).

37. Stern, E.A., Sayers, D.E. and Lytle, F.W., Phys. Rev. B$\underline{11}$, 4836 (1975).

38. Teo, B., Lee, P.A., Simons, A.L., Eisenberger, P. and Kincaid, B.M., J. Am. Chem. Soc. $\underline{99}$, 3854 (1977).

39. von Heimendahl, L. and Thorpe, M.F., J. Phys. F$\underline{5}$, L87 (1975).

40. Weaire, D., Ashley, M.F., Logan, J. and Weins, M.J., Acta Metal-lurgica $\underline{19}$, 773 (1971).

41. Weaire, D. and Thorpe, M.F., Phys. Rev. B$\underline{4}$, 2508 (1971).

42. Zachariansen, W.H., J. Amer. Chem. Soc. $\underline{54}$, 3841 (1932).